ORIGINAL PAPER

Three-dimensional nonlinear vibration model and fatigue failure mechanism of deepwater test pipe

Xiaoqiang Guo · Yuxin Nie · Jun Liu · Yufa He · Liangjie Mao · Guorong Wang · Liming Dai

Abstract In deepwater test condition, the riser–test pipe (tubing string) system (RTS) is subject to the vortex-induced effect on riser, flow-induced effect on test pipe and longitudinal/transverse coupling effect, which is prone to buckling deformation, fatigue fracture and friction perforation. To resolve this, the three-dimensional (3D) nonlinear vibration model of deepwater RTS is established using the micro-finite method, energy method and Hamilton variational principle. Based on the elastic–plastic contact collision theory, the nonlinear contact load calculation method between riser and test pipe is proposed. Compared with experimental measurement results, calculation results using the proposed vibration model in this study and the single tubing vibration model in our recent work, the correctness and effectiveness of the proposed vibration model of the deepwater RTS are verified. Meanwhile, the cumulative damage theory is used to establish the fatigue life prediction method of test pipe. Based on that, the influences of outflow velocity, internal flow velocity, significant wave height, as well as top tension coefficient on the fatigue life of test pipe are systematically analyzed. The results demonstrate that, first, with the increase in outflow velocity, the maximum alternating stress and the annual fatigue damage rate increased. The location where fatigue failure of the test pipe is easy to occur at the upper "one third" and the bottom of test pipe are easy to occur fatigue failure. Second, with the increase in internal flow velocity, the "one third damage effect" of the test pipe will decrease, and the "bottom damage effect" of the test pipe increased that needs the attention of field operators. Third, during field operation, it is necessary to properly configure the top tension coefficient so that there can be a certain relaxation between the riser and the test pipe, so as to cause transverse vibration and consume some axial energy and load. The study led to a theoretical method for safety evaluation and a practical approach for effectively improving the fatigue life of deepwater test pipe.

X. Guo (✉) · Y. Nie · J. Liu (✉) · G. Wang
School of Mechatronic Engineering, Southwest Petroleum University, Chengdu 610500, China
e-mail: 786526101@qq.com

J. Liu
e-mail: 201031010081@swpu.edu.cn

X. Guo
School of Mechanical Engineering, Hebei University of Technology, Tianjin 300401, China

X. Guo · L. Dai
Industrial Systems Engineering, University of Regina, Regina, SK S4S 0A2, Canada

Y. He · L. Mao · G. Wang
Energy Equipment Institute, Southwest Petroleum University, Chengdu 610500, China

Y. He
CNOOC Research Institute Co., Ltd., Beijing 100028, China

List of symbols

$v_i, i = x, y, z$	Displacement components of riser, m
$v_i'', i = x, y, z$	Second derivative of riser displacements versus z
E	Elastic modulus of the RTS, Pa
I_v	Polar moment of inertia of the riser, m^4
ρ_v	Density of the riser, kg/m^3
$F_x(z, t)$	Contact/impact force of riser–test pipe in x-directions, N
$F_L(z, t)$	Lateral lift in the CF direction, N
ζ	Structural damping ratio
ω_v	Natural angular frequency of riser
L_v	Length of riser, m
D_o	Riser outer diameter, m
m_i	The mass of the gas per unit length (kg)
$S_i, i = x, y, z$	Displacement components of the test pipe, m
$S_i'', i = x, y, z$	Second derivative of test pipe displacements versus z
$f_x(z, t)$	High-speed fluid impact load in test pipe in x-direction, N
$f_z(z, t)$	High-speed fluid impact load in test pipe in z-direction, N
ω_s	Natural angular frequency of test pipe
$w_s(= m_s g)$	Weight of test pipe per unit length, N
V_r	Relative velocity between the fluid and the riser, m/s
U_c	Outflow velocity of the riser, m/s
F_D', C_D	Component forces of the fluctuating drag force and corresponding coefficient
F_L', C_L	Fluctuating lift force and corresponding coefficient
S_t	Strouhal number
R_1	Radius of riser, m
f_F	The friction of RTS, N
E	Elastic modulus of the riser or test pipe material, Pa
ρ_i	Density of gas in the test pipe, kg/m^3
$\alpha(t)$	Deflection angles of test pipe in x-direction, rad
$\alpha(s)$	Inclination angle, rad
K_U	Rotational stiffness of the upper flexible joint
$u_{\text{boat}}(t)$	Heave displacement of the platform, m
m_p	Mass of platform, kg
$\eta(t)$	Surface displacement of random wave, m
$\hat{\omega}_i$	Circular frequency of the ith harmonic, Hz
a_i	Amplitude of the ith harmonic component, m
$S(\omega)$	Random wave spectrum
ω	Circular frequency, Hz
$T_{1/3}$	Significant period of the wave, s
T_p	Peak period of the wave, s
σ	Peak shape coefficient
$F_p(t)$	Exciting force of the random wave on the heave plate, N
$J_1(\cdot)$	First-order Bessel function of first kind
z_{plate}	Depth of heave plate, m
$\mathbf{d}$	Displacement vector of riser unit
$\varphi_i, i = x, y, z$	Vibration shape function of riser and test pipe unit
$\mathbf{F}(t)$	Load column vector
$\mathbf{M}(t)$	Matrices of the overall mass
ρ_p	Density of the actual RTS, kg/m^3
ρ_m	Density of the RTS in the simulation experiment
λ	Radial similarity ratio
C_L	Load-type correction factor
K_f	Stress concentration correction factor
C_S	Surface quality correction factor
S_e	Corrected stress, Pa
$v_i', i = x, y, z$	First-order derivative of riser displacements versus z
$\dot{v}_i, i = x, y, z$	First-order derivative of riser displacements versus time
A_v	Cross-sectional area of the riser, m^2
$F_z(z, t)$	Friction force of riser–test pipe in z-directions, N
m_v	Mass of the per unit length riser, kg
$F_y(z, t)$	Contact/impact force of riser–test pipe in y-directions, N
$F_D(z, t)$	Drag force in the IL direction, N
$c_v(= 2m_v \omega_v \zeta)$	Structural damping coefficient of riser

w_g	Buoyant weight of riser per unit length, N
ρ_w	Density of the seawater, kg/m^3
A_s	Cross-sectional area of the test pipe, m^2
m_s	Mass of the per unit length test pipe, kg
$S'_i, i = x, y, z$	First-order derivative of test pipe displacements versus z
$\dot{S}_i, i = x, y, z$	First-order derivative of test pipe displacements versus time
$f_y(z, t)$	High-speed fluid impact load in test pipe in y-direction, N
$c_s(=2m_s\omega_s\zeta)$	Structural damping coefficient of test pipe
$v_i, i = x, y, z$	Absolute velocities of the internal high-speed fluid (m/s)
V	Fluid flow velocity in the test pipe, m/s
$\overline{C}_d$	Coefficient of steady-state drag force
$\overline{C}_l$	Coefficient of steady lift force
$q_i, i = x, y$	Dimensionless wake oscillator variables in IL and CF directions
δ	The relative deformation between riser and test pipe, m
ω'_s	Vortex shedding frequency
R_2	Radius of test pipe, m
F	Contact load of riser–test pipe, N
ξ	Friction coefficient between the riser and test pipe
A_i	Cross-sectional area of the wellbore, m^2
$\varphi(t)$	Deflection angles of test pipe in y-direction, rad
$\varphi(s)$	Azimuth, rad
K_L	Rotation stiffness of the BOP
$B_i, i = 1, 2$	Heave radiation and heave viscous damping
A_w	Area of the platform at sea level, m^2
$\overline{F}_z$	Random heave wave exciting force on platform, N
ε_i	Initial phase of the ith harmonic component, rad
$\Delta\omega$	Frequency step
f	Frequency, Hz
$H_{1/3}$	Significant wave height, m
f_p	Peak frequency of the wave, Hz
γ	Peak parameter

R	Platform radius, m
$F_s(t)$	Exciting force of the random wave on the platform body, N
d	Draft of platform, m
B_{plate}	Width of heave plate, m
$\overline{\mathbf{d}}$	Displacement vector of test pipe unit
$\mathbf{D}$	Matrix of overall displacement
$\mathbf{K}(t)$	Matrices of the overall stiffness
$\mathbf{C}(t)$	Matrices of the overall damping
E_p	Elastic modulus of the actual RTS, Pa
E_m	Elastic modulus of the RTS in the simulation experiment
T_f	Service life of test pipe, year
C_D	Test specimen size correction factor
R_a	Surface roughness of the specimen, μm
S_{be}	Standard stress, Pa
D'	Total fatigue damage

Abbreviations

RTS	Riser–test pipe system
VIV	Vortex-induced vibration
CF	Cross-flow
BOP	Blowout preventer
LMRP	Lower marine riser packing
3D	Three-dimensional
CFD	Computational fluid dynamics
IL	Inline
RMS	Root mean square

1 Introduction

With the increasing demand for oil and gas resources in the world, the exploitation trend of offshore oil and gas resources gradually develops from shallow water (water depth is less than 500 m) to deep water. (Water depth is between 500 and 1500 m.) The riser–test pipe system (RTS) is the core equipment for deepwater oil and gas exploitation, but which is subject to the vortex-induced effect on riser, flow-induced effect on test pipe and longitudinal/transverse coupling effect. The RTS is prone to buckling deformation, fatigue fracture and friction perforation, so which is the weakest equipment. Compared with conventional water depth testing conditions, the RTS is subjected to greater risks in deepwater test conditions. These risks are mainly caused by severe non-periodic vibrations of the RTS induced by the vortex-induced effect on riser, flow-

induced effect on test pipe, nonlinear contact/collision of the tube in tube and longitudinal/transverse coupling effect, thereby making the RTS more susceptible to buckling deformation (Fig. 1a), fatigue fracture (Fig. 1b) and friction perforation (Fig. 1c) [1]. Once the system structure is damaged, it will lead to serious offshore oil and gas accidents, resulting in significant economic losses and environmental pollution. Therefore, the three-dimensional (3D) nonlinear vibration model and fatigue failure mechanism for deepwater RTS should be investigated. Finally, the research results can provide a theoretically sound guidance for designing and practically sound approach for effectively improving the service life of test pipe.

Aiming at the problem of riser vibration, the most work focused on the vortex-induced vibration (VIV) of rigid cylinders [2, 3], in which the general VIV mechanism and law were obtained, such as the frequency-locked phenomenon [4] and lagging behavior [5]. In recent years, driven by offshore oil and gas exploitation, more and more attention has been paid to the VIV problem of flexible cylinders in which the aspect ratio is a very important parameter. Physical experiments [6–8] and computational fluid dynamics (CFD) numerical simulations [9–12] are the two most common methods in these studies, and remarkable progress was made. However, when the aspect ratio of a cylinder is large or a solid model is used, physical experiments usually become very expensive and impractical, and it is difficult to analyze the vibration of the riser by CFD numerical simulation, including the inability to achieve higher accuracy and faster calculation efficiency. Therefore, in the VIV study of risers, there are relatively few works that consider a large aspect ratio (the ratio of length to diameter is greater than 1000) or the actual size. In addition to a large aspect ratio, the impact of the ocean environment

load on the VIV behavior of a riser is significant. The VIV response mechanism of a flexible riser under shear flow was examined by Mathelin et al. [13] using a wake oscillator model presented by Facchinetti et al. [5]. Since the VIV amplitude in the cross-flow (CF) direction is larger than that in the inline (IL) direction, most work has focused on the VIV in the CF direction [14]. The effects of the flow velocity, top tension and pipe diameter on VIV behavior in the cross-flow direction of a riser were studied by Xu et al. [15] and He et al. [16] using a VIV model. In the above studies, the VIV behavior in the IL direction and its influence were not taken into account. However, it was found in the work of Jauvtis and Williamson [17] that as the mass ratio (the ratio of the structural quality to the mass of discharged fluid) was less than 6.0, the IL vibration of a cylinder could not be neglected. The VIV characteristics study of a rigid cylinder presented by Gu et al. [18], Martins et al. [19] and Gao et al. [20] also showed that the effect of the IL vibration was significant. In our recent work [21, 22], the response characteristics of VIV of marine risers with consideration of the coupling effects of the CF and IL vibration were investigated. It was found that there are the frequency locking effect in the uniform flow and the multi-frequency effect in the shear flow for the IL vibration.

The deepwater test pipe and tubing string represent the same kind of tubular structure. The deepwater test pipe is the name of the tubular structure under the test condition, and the tubing string is the name of the tubular structure under the production condition. Therefore, their vibration characteristics have the same trend, which are nonlinear vibration induced by inside flow. Aiming at the flow-induced vibration of tubular structure, firstly, some scholars [23, 24] have verified the phenomenon that the internal fluid can

(a) Buckling deformation   (b) Fatigue fracture   (c) Friction perforation
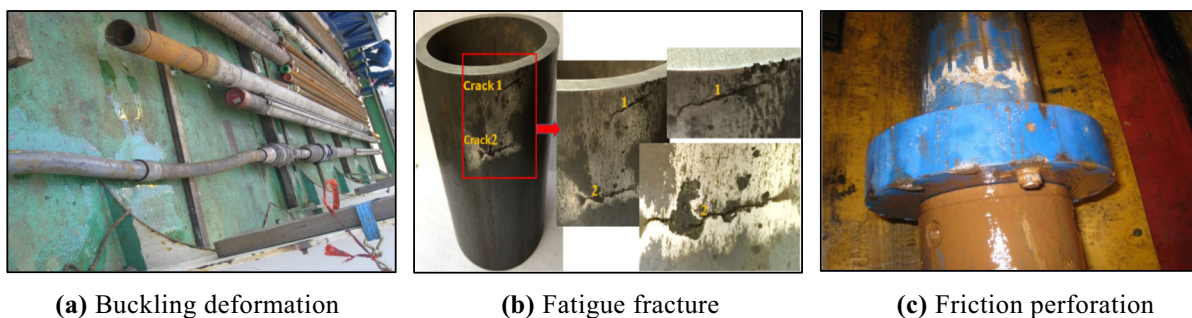
Fig. 1 Failure forms of the riser–test pipe system (RTS)

induce the vibration of the tubular structure through experiments, which points out the direction for the later scholars' research. However, the calculation method of interaction force and the vibration model of the tubular structure are not obtained. Subsequently, many scholars carried out detailed research on the calculation method of interaction force and the vibration model and established the calculation method of fluid force [25], the string vertical vibration [26, 27], the lateral vibration [28, 29] and the fluid–structure coupled vibration model [30, 31]. However, the above models mainly focus on the vibration in a single direction, which can effectively predict the vibration of tubular structure with small aspect ratio, and its calculation accuracy decreased to predict the vibration of tubular structure with large aspect ratio. Also, some scholars [32–34] found that the longitudinal/lateral coupling effects of tubular structure with large aspect ratio cannot be ignored. Therefore, in our recent work [21, 22], the longitudinal/lateral coupling model of marine risers with consideration of the coupling effects of the CF and IL vibration was established. In the actual operation process, there are other structures outside the tubing string to restrict its vibration, resulting in the structure of pipe in pipe. Therefore, the contact/collision between pipes is also one of the important factors in tubing string modeling. This research was attracted the interest of some scholars and they carried out corresponding research, in which the bracing effect of the outer pipe was taken into account by some researchers [35, 36] to analyze the static buckling deformation of the tubing string. Meanwhile, the commercial software was used by researchers [37, 38] to investigate the impact force/friction force in the flow-induced vibration of slender structures in vertical well. Also, in our recent work [39, 40], the flow-induced nonlinear vibration model of tubing string in conventional oil and gas wells was established, which considers the longitudinal/lateral coupling effect of tubing string and the nonlinear contact collision effect of tubing–casing. In summary, the interaction between riser and test pipe is ignored in the above studies, which make the calculation results by the single vibration model not in accordance with the actual.

The vibration failure of tubular structure has been paid attention to by scholars, mainly including wear failure, fatigue failure and insufficient strength failure [41]. In this work, the vibration fatigue failure of

deepwater RTS is mainly studied. Therefore, the current research on fatigue failure of tubular structure investigated and analyzed. Lekkala et al. [42] established a fatigue life prediction model of riser using SHEAR7 commercial software and provided the new optimized excitation coefficient datasets, which reduce the error in the predicting the VIV response of the riser. Chen et al. [43] analyzed root cause of tubing and casing failures in low-temperature carbon dioxide injection well, and an optimal tubing–casing combination is proposed to prolong the operation life of tubing. Moreover, in view of the fatigue failure of the risers caused by VIV, the researchers established a fatigue life prediction method for risers in deep water [44, 45]. However, in their method, the acquisition of alternating stress ignores the contact and collision factors between riser and test pipe, which makes it impossible to accurately simulate the fatigue life of riser under severe working conditions.

Above all, the existing deepwater riser vibration research mainly focuses on the VIV of a single riser, and a few scholars studied the riser–drill string coupling vibration. However, in the test condition, the research on the coupling vibration of the RTS has not be reported. The establishment of corresponding vibration model and the revelation of fatigue failure mechanism can effectively ensure the safety of RTS. Therefore, in this study, the 3D nonlinear vibration model of deepwater RTS is established, in which the vortex-induced effect of riser, the heave motion of platform, the flow-induced effect of test pipe and the nonlinear contact effect of double pipe were taken into account. Then, the incremental form of Newmark-β and Newton–Raphson is used to solve the 3D nonlinear vibration model. Meanwhile, a vibration test bench for the RTS is designed using similarity principle, and the correctness and effectiveness of the proposed 3D nonlinear vibration model are verified by comparing with experimental data. Moreover, the cumulative damage theory is used to establish the fatigue life prediction method of test pipe combined with the stress response, which was determined by the proposed model and the S–N curve of the pipe material (13Cr-L80) which was measured by fatigue test. Finally, the influences of outflow velocity, internal flow velocity, significant wave height, as well as top tension coefficient on the fatigue life of test pipe are systematically analyzed.

2 3D nonlinear vibration model of the RTS

2.1 Nonlinear vibration control equation of the RTS

In this section, the 3D vibration control equations of infinitesimal riser–test pipe (RTS) were established through the energy method and Hamilton variational principle. Owing to the infinitesimal segment of the RTS which is very short, it can be regarded as a straight segment. Therefore, a coordinate system is established in which the depth direction set as z-axis, the horizontal direction (the IL direction) set as x-axis and the y-axis (the CF direction) satisfy the right-hand rule (Fig. 2). The following basic assumptions are made before modeling.

(1) The material mechanical property of riser and test pipe is ideal isotropic and elastic.
(2) The gravity and frictional resistance are evenly distributed on the tubing element.
(3) The test pipe axis is coincided with the riser axis at initial moment, and the gravity of the RTS acts on itself at initial moment.
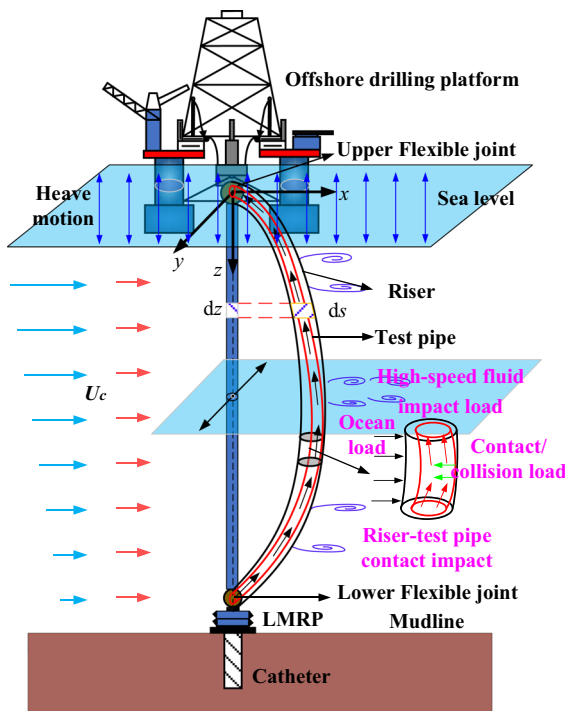

Fig. 2 Structure diagram of the RTS

(4) The friction coefficient at each location of the system is constant.

2.1.1 Vibration control equation of riser

Based on the small deformation hypothesis and the Kirchhoff hypothesis [22], the three displacement field components u_1, u_2 and u_3 along the coordinates x, y and z, respectively, can be written as:

$$\begin{cases} u_1(z,t) = v_x(z,t), u_2(z,t) = v_y(z,t) \\ u_3(z,x,t) = v_z(z,t) - x\dfrac{\partial v_x(z,t)}{\partial z} - y\dfrac{\partial v_y(z,t)}{\partial z} \end{cases} \quad (1)$$

where v_x, v_y and v_z represent the displacement components of any section in the riser on the three coordinate axes, respectively (m).

According to Zhao's work [46], the Green strain can be expressed as follows:

$$\begin{cases} \varepsilon_{xx} = \dfrac{\partial u_1}{\partial x}, \ \varepsilon_{yy} = \dfrac{\partial u_2}{\partial y}, \ \varepsilon_{zz} = \dfrac{\partial u_3}{\partial z} + \dfrac{1}{2}\left[\left(\dfrac{\partial u_1}{\partial z}\right)^2 + \left(\dfrac{\partial u_2}{\partial z}\right)^2\right] \\ \varepsilon_{xz} = \dfrac{1}{2}\left(\dfrac{\partial u_1}{\partial z} + \dfrac{\partial u_3}{\partial x}\right), \ \varepsilon_{yz} = \dfrac{1}{2}\left(\dfrac{\partial u_2}{\partial z} + \dfrac{\partial u_3}{\partial y}\right) \ \varepsilon_{xy} = \dfrac{1}{2}\left(\dfrac{\partial u_1}{\partial y} + \dfrac{\partial u_2}{\partial x}\right) \end{cases}$$
$$(2)$$

Substituting Eq. (1) into Eq. (2), the following equation can thus be obtained:

$$\begin{cases} \varepsilon_{zz} = \dfrac{\partial v_z}{\partial z} - x\dfrac{\partial^2 v_x}{\partial z^2} - y\dfrac{\partial^2 v_y}{\partial z^2} + \dfrac{1}{2}\left[\left(\dfrac{\partial v_x}{\partial z}\right)^2 + \left(\dfrac{\partial v_y}{\partial z}\right)^2\right] \\ \varepsilon_{xx} = \varepsilon_{yy} = \varepsilon_{xz} = \varepsilon_{yz} = \varepsilon_{xy} = 0 \end{cases}$$
$$(3)$$

Based on the second Kirchhoff stress and neglecting Poisson effect, Hooke's law under uniaxial stress state is written as:

$$\sigma_{zz} = E\varepsilon_{zz} \quad (4)$$

Since the infinitesimal segment of the tubing is a standard cylinder, the integral satisfies the following formula:

$$\int_A x\mathrm{d}A = \int_A y\mathrm{d}A = \int_A (xy)\mathrm{d}A = 0, \quad \int_A x^2\mathrm{d}A$$
$$= \int_A y^2\mathrm{d}A = I \quad (5)$$

According to elastic–plastic mechanics [47] and Eqs. (1)–(5), the total kinetic energy T, potential energy U and energy with external force W of the riser can be, respectively, expressed as:

$$
\begin{cases}
T = \int_0^L \int_A \dfrac{\rho_v}{2}\left(\dot{u}_1^2 + \dot{u}_2^2 + \dot{u}_3^2\right)\mathrm{d}A\mathrm{d}z = \dfrac{1}{2}\int_0^L\left[m_v\left(\dot{v}_x^2 + \dot{v}_y^2 + \dot{v}_z^2\right) + \rho_v I_v\left(\dot{v}_x'^2 + \dot{v}_y'^2\right)\right]\mathrm{d}z \\[2mm]
U = \dfrac{1}{2}\int_V \sigma\varepsilon\,\mathrm{d}V = \dfrac{E}{2}\int_V \varepsilon_{zz}^2\,\mathrm{d}V = \dfrac{1}{2}\int_0^L\left\{EA_v\left[v_z' + \dfrac{1}{2}\left(v_x'^2 + v_y'^2\right)\right]^2 + EI_v\left(v_x''^2 + v_y''^2\right)\right\}\mathrm{d}z \\[2mm]
W = \int_0^L\left[(F_D(z,t)+F_x(z,t)-c_v\dot{v}_x)\mathrm{d}v_x + (F_L(z,t)+F_y(z,t)-c_v\dot{v}_y)\mathrm{d}v_y + (F_z(z,t)+w_g-c_v\dot{v}_z)\mathrm{d}v_z\right]\mathrm{d}z
\end{cases} \tag{6}
$$

where E is the elastic modulus of the riser and test pipe (Pa); A_v is the cross-sectional area of the riser (m²); v_i', $i = x, y, z$, v_i'', $i = x, y, z$ are the first-order and second derivative of riser displacements versus z, respectively; $\dot{v}_i$, $i = x, y, z$ is the first-order derivative of riser displacements versus time in x-, y- and z-directions (m/s); m_v is the mass of the per unit length riser (kg); ρ_v is the density of the riser (kg/m³); I_v is the polar moment of inertia of the riser (m⁴); $F_x(z,t)$, $F_y(z,t)$, $F_z(z,t)$ are the contact/impact and friction force of riser–test pipe in x-, y- and z-directions (N), which can be determined in Sect. 2.2; $F_D(z,t)$, $F_L(z,t)$ are the drag force in the IL direction and the lateral lift in the CF direction (N), which also can be determined in Sect. 2.2; $c_v(=2m_v\omega_v\zeta)$ is the structural damping coefficient of riser (ω_v is natural angular frequency of riser, $\omega_v = \pi^2\sqrt{EI_v/\left(m_v L_v^4\right)}$, L_v is the length of riser (m); ζ is structural damping ratio); and $w_g\left(= m_v g - \rho_w \pi D_o^2/4\right)$ is buoyant weight of riser per unit length (N) (ρ_w the density of the sea-water (kg/m³); D_o is the riser outer diameter (m)).

For a riser section with length $\mathrm{d}z$, its length $\mathrm{d}s$ after deformation can be written as follows:

$$
\mathrm{d}s = \sqrt{1 + v_x'^2 + v_y'^2}\,\mathrm{d}z \tag{7}
$$

Therefore, the longitudinal strain and its variation of the riser can be written, respectively, as

$$
v_z' = \varepsilon_0 + \frac{\mathrm{d}s - \mathrm{d}z}{\mathrm{d}z} \cong \varepsilon_0 + \frac{1}{2}\left(v_x'^2 + v_y'^2\right) \Rightarrow \delta v_z' = v_x'\delta v_x' + v_y'\delta v_y' \tag{8}
$$

According to variational principle $(\delta U|_{t=t_{1,2}/x=0,L.} = \delta U'|_{t=t_{1,2}/x=0,L} = \delta\dot{U}|_{t=t_{1,2}/x=0,L} = 0)$ and integration by parts $(\int[f'(z)g(z)]\mathrm{d}z = f(z)g(z) - \int[f(z)g'(z)]\mathrm{d}z)$, the integration forms of T, U and W over time can be expressed as:

$$
\begin{aligned}
\delta\int_{t_1}^{t_2} T\,\mathrm{d}t &= \frac{1}{2}\delta\int_{t_1}^{t_2}\int_0^L\left[m_v\left(\dot{v}_x^2 + \dot{v}_y^2 + \dot{v}_z^2\right) + \rho_v I_v\left(\dot{v}_x'^2 + \dot{v}_y'^2\right)\right]\mathrm{d}z\mathrm{d}t \\
&= \int_{t_1}^{t_2}\int_0^L\left[m_v\left(\dot{v}_x\delta\dot{v}_x + \dot{v}_y\delta\dot{v}_y + \dot{v}_z\delta\dot{v}_z\right) + \rho_v I_v\left(\dot{v}_x'\delta\dot{v}_x' + \dot{v}_y'\delta\dot{v}_y'\right)\right]\mathrm{d}z\mathrm{d}t \\
&= \int_0^L\left[\begin{array}{l} m_v\left(\left(\dot{v}_z\delta v_z + \dot{v}_z\delta v_z + \dot{v}_z\delta v_z\right)\big|_{t_1}^{t_2} - \int_{t_1}^{t_2}\left(\ddot{v}_x\delta v_x + \ddot{v}_y\delta v_y + \ddot{v}_z\delta v_z\right)\mathrm{d}t\right) \\ +\rho_v I_v\left(\left(\dot{v}_x'\delta v_x' + \dot{v}_y'\delta v_y'\right)\big|_{t_1}^{t_2} - \int_{t_1}^{t_2}\left(\ddot{v}_x'\delta v_x' + \ddot{v}_y'\delta v_y'\right)\mathrm{d}t\right)\end{array}\right]\mathrm{d}z \\
&= -\int_0^L\int_{t_1}^{t_2} m_v\left(\ddot{v}_x\delta v_x + \ddot{v}_y\delta v_y + \ddot{v}_z\delta v_z\right)\mathrm{d}t\mathrm{d}z - \rho_v I_v\int_{t_1}^{t_2}\int_0^L\left(\ddot{v}_x'\mathrm{d}\delta v_x + \ddot{v}_y'\mathrm{d}\delta v_y\right)\mathrm{d}t \\
&= -\int_0^L\int_{t_1}^{t_2} m_v\left(\ddot{v}_x\delta v_x + \ddot{v}_y\delta v_y + \ddot{v}_z\delta v_z\right)\mathrm{d}t\mathrm{d}z - \rho_v I_v\int_{t_1}^{t_2}\left[\left(\ddot{v}_x'\delta v_x + \ddot{v}_y'\delta v_y\right)\big|_0^L - \int_0^L\left(\ddot{v}_x''\delta v_x + \ddot{v}_y''\delta v_y\right)\mathrm{d}z\right]\mathrm{d}t \\
&= \int_{t_1}^{t_2}\int_0^L\left[-m_v\left(\ddot{v}_x\delta v_x + \ddot{v}_y\delta v_y + \ddot{v}_z\delta v_z\right) + \rho_v I_v\left(\ddot{v}_x''\delta v_x + \ddot{v}_y''\delta v_y\right)\right]\mathrm{d}z\mathrm{d}t
\end{aligned} \tag{9}
$$

$$\delta \int_{t_1}^{t_2} U \mathrm{d}t = \frac{1}{2} \delta \int_{t_1}^{t_2} \int_0^L \left[EA_v \left(v_z' + \frac{1}{2} \left(v_x'^2 + v_y'^2 \right) \right)^2 + EI_v \left(v_x''^2 + v_x''^2 \right) \right] \mathrm{d}z \mathrm{d}t$$

$$= \int_{t_1}^{t_2} \int_0^L \left[EA_v \left(v_z' + \frac{1}{2} \left(v_x'^2 + v_y'^2 \right) \right) \left(\delta v_z' + v_x' \delta v_x' + v_y' \delta v_y' \right) + EI_v \left(v_x'' \delta v_x'' + v_y'' \delta v_y'' \right) \right] \mathrm{d}z \mathrm{d}t$$

$$= EA_v \int_{t_1}^{t_2} \left\{ \left[\left(v_z' + \frac{1}{2} \left(v_x'^2 + v_y'^2 \right) \right) \cdot \left(\delta v_z + v_x' \delta v_x + v_y' \delta v_y \right) \right] \Big|_0^L - \int_0^L \left[\begin{array}{c} \left(v_z' + \frac{1}{2} \left(v_x'^2 + v_y'^2 \right) \right)' \delta v_z + \\ \left[\left(v_z' + \frac{1}{2} \left(v_x'^2 + v_y'^2 \right) \right) v_x' \right]' + \left[\left(v_z' + \frac{1}{2} \left(v_x'^2 + v_y'^2 \right) \right) v_y' \right]' \end{array} \right] \mathrm{d}z \right\} \mathrm{d}t$$

$$+ EI_v \int_{t_1}^{t_2} \left\{ \left(v_x'' \delta v_x' + v_y'' \delta v_y' \right) \Big|_0^L - \int_0^L \left[\left(v_x'' \right)' \mathrm{d}\delta v_x + \left(v_y'' \right)' \mathrm{d}\delta v_y \right] \right\} \mathrm{d}t$$

$$= -EA_v \int_{t_1}^{t_2} \int_0^L \left[\left(v_z' + \frac{1}{2} \left(v_x'^2 + v_y'^2 \right) \right)' \delta v_z + \left[\left(v_z' + \frac{1}{2} \left(v_x'^2 + v_y'^2 \right) \right) v_x' \right]' + \left[\left(v_z' + \frac{1}{2} \left(v_x'^2 + v_y'^2 \right) \right) v_y' \right]' \right] \mathrm{d}z \mathrm{d}t$$

$$+ EI_v \int_{t_1}^{t_2} \left\{ \left(v_x'' \delta v_x' + v_y'' \delta v_y' \right) \Big|_0^L - \left[\left(v_x'' \right)' \mathrm{d}\delta v_x + \left(v_y'' \right)' \mathrm{d}\delta v_y \right] \Big|_0^L + \int_0^L \left[\left(v_x'' \right)'' \delta v_x + \left(v_y'' \right)'' \delta v_y \right] \mathrm{d}z \right\} \mathrm{d}t$$

$$= -EA_v \int_{t_1}^{t_2} \int_0^L \left[\left(v_z' + \frac{1}{2} \left(v_x'^2 + v_y'^2 \right) \right)' \delta v_z + \left[\left(v_z' + \frac{1}{2} \left(v_x'^2 + v_y'^2 \right) \right) v_x' \right]' + \left[\left(v_z' + \frac{1}{2} \left(v_x'^2 + v_y'^2 \right) \right) v_y' \right]' \right] \mathrm{d}z \mathrm{d}t$$

$$+ EI_v \int_{t_1}^{t_2} \int_0^L \left[\left(v_x'' \right)'' \delta v_x + \left(v_y'' \right)'' \delta v_y \right] \mathrm{d}z \mathrm{d}t$$

(10)

$$\delta \int_{t_1}^{t_2} W \mathrm{d}t = \int_{t_1}^{t_2} \int_0^L \left[\binom{F_D(z,t)+}{F_x(z,t) - c\dot{v}_x} \delta v_x \right. \\ \left. + \binom{F_L(z,t)+}{F_y(z,t) - c\dot{v}_y} \delta v_y + \binom{F_z(z,t)+}{w_g - c\dot{v}_z} \delta v_z \right] \mathrm{d}z \mathrm{d}t$$

(11)

Substituting Eqs. (9)–(11) into the expression of Hamiltonian principle $\delta \int_{t_1}^{t_2} (U - T + W) \mathrm{d}t = 0$, the nonlinear vibration control equations of the riser can be obtained and expressed as follows:

2.1.2 Vibration control equation of test pipe

In the oil and gas test condition, the test pipe is located inside the riser, forming a pipe in pipe structure, and there exist high-speed test oil and gas in the test pipe. Therefore, the main factors causing the nonlinear vibration of the test pipe include the contact/collision of the external riser and the impact of the internal high-speed oil and gas. In this study, the same coordinate system as riser was established. Based on the assumption of Eq. (1) and Green's strain, the expres-

$$\begin{cases} m_v \ddot{v}_x + c\dot{v}_x - \rho_v I_v \ddot{v}_x'' - EA_v \left(\left(v_z' + \frac{1}{2} \left(v_x'^2 + v_y'^2 \right) \right) v_x' \right)' + EI_v \left(v_x'' \right)'' = F_D(z,\ t) + F_x(z,\ t) \\ m_v \ddot{v}_y + c\dot{v}_y - \rho_v I_v \ddot{v}_y'' - EA_v \left(\left(v_z' + \frac{1}{2} \left(v_x'^2 + v_y'^2 \right) \right) v_y' \right)' + EI_v \left(v_y'' \right)'' = F_L(z,\ t) + F_y(z,\ t) \\ m_v \ddot{v}_z + c\dot{v}_z - EA \left(v_z'' + \frac{1}{2} \left(v_x'^2 + v_y'^2 \right)' \right) = F_z(z,\ t) + w_g \end{cases}$$

(12)

sions of strain energy, kinetic energy and work done can be obtained as follows, and the kinetic energy of the fluid in the pipe is considered.

in Sect. 2.2; $c_s(=2m_s\omega_s\zeta)$ is the structural damping coefficient of test pipe (ω_s is natural angular frequency of test pipe); $w_s(=m_sg)$ is weight of test pipe per unit

$$\begin{cases} \overline{T} = \dfrac{1}{2}\int_0^L \left[m_s\left(\dot{S}_x^2 + \dot{S}_y^2 + \dot{S}_z^2\right) + \rho_s I_s\left(\dot{S}_x'^2 + \dot{S}_y'^2\right) + m_i\left(v_x^2 + v_y^2 + v_z^2\right) \right]\mathrm{d}z \\[2mm] \overline{U} = \dfrac{1}{2}\int_0^L \left[EA_s\left(S_z' + \dfrac{1}{2}\left(S_x'^2 + S_y'^2\right)\right)^2 + EI_s\left(S_x''^2 + S_y''^2\right) \right]\mathrm{d}z \\[2mm] \overline{W} = \int_0^L \left(\begin{pmatrix} F_x(x,t)+ \\ f_x(x,t) - c_s\dot{S}_x \end{pmatrix}\mathrm{d}S_x + \begin{pmatrix} F_y(x,t)+ \\ f_y(x,t) - c_s\dot{S}_y \end{pmatrix}\mathrm{d}S_y + \begin{pmatrix} F_z(x,t) + f_z(x,t) \\ + w_s - c_s\dot{S}_z \end{pmatrix}\mathrm{d}S_z \right)\mathrm{d}z \end{cases} \tag{13}$$

where S_x, S_y and S_z are the displacement components of any section in the test pipe on the three coordinate axes, respectively (m); m_s and m_i are the masses of the per unit length test pipe and the gas per unit length (kg), respectively; A_s is the cross-sectional area of the test pipe (m^2); S_i', $i = x, y, z$ and S_i'', $i = x, y, z$ are the first-order and second derivative of test pipe displacements versus z, respectively; $\dot{S}_i$, $i = x, y, z$ is the first-order derivative of test pipe displacements versus time in x-, y- and z-directions (m/s); $f_x(z,t)$, $f_y(z,t)$, $f_z(z,t)$ are the high-speed fluid impact load in test pipe in x-, y- and z-directions (N), which also can be determined

length (N); and v_x, v_y and v_z are the absolute velocities of the internal high-speed fluid in x-, y- and z-directions (m/s), respectively, which can be expressed as follows:

$$v_x = \dot{S}_x + VS_x', v_y = \dot{S}_y + VS_y', v_z = V \tag{14}$$

where V is the fluid flow velocity in the test pipe (m/s). Also, substituting Eqs. (13) and (14) into the expression of Hamiltonian principle, the nonlinear vibration control equations of test pipe can be expressed as follows:

$$\begin{cases} (m_s + m_i)\ddot{S}_x - \rho_s I_s\ddot{S}_x'' + 2m_iV\dot{S}_x' + c_s\dot{S}_x + m_iV^2S_x'' + EI_s\left(S_x''\right)'' - EA\left(\left(S_z' + \dfrac{1}{2}\left(S_x'^2 + S_y'^2\right)\right)S_x'\right)' = F_x(z,t) + f_x(x,t) \\[2mm] (m_s + m_i)\ddot{S}_y - \rho_s I_s\ddot{S}_y'' + 2m_iV\dot{S}_y' + c_s\dot{S}_y + m_iV^2S_y'' + EI_s\left(S_y''\right)' - EA\left(\left(S_z' + \dfrac{1}{2}\left(S_x'^2 + S_y'^2\right)\right)S_y'\right)' = F_y(z,t) + f_y(x,t) \\[2mm] m_s\ddot{S}_z + c_s\dot{S}_z - EA\left(S_z'' + \dfrac{1}{2}\left(S_x'^2 + S_y'^2\right)'\right) = F_z(z,t) + f_z(x,t) + w_s \end{cases} \tag{15}$$

Fig. 3 External fluid forces acting on the riser
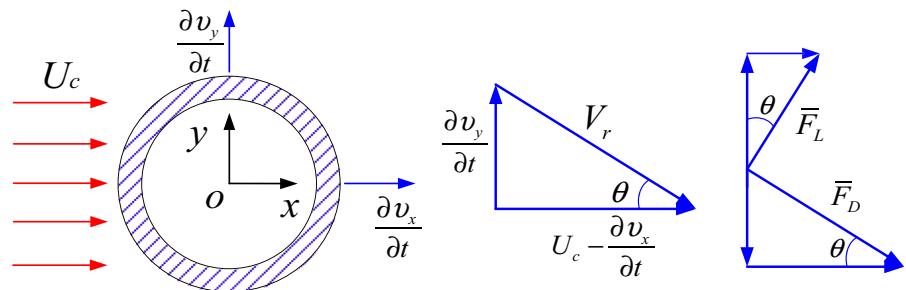
2.2 Boundary conditions

In the deepwater test condition, the external loads on the RTS include the ocean environment load and the high-speed fluid impact load. The internal loads are the nonlinear contact collision between the riser and test pipe. The upper part of the RTS is connected with the drilling platform, and the lower part is connected with the blowout preventer (BOP). Thus, the upper displacement boundary considers the heave motion of the platform, and the lower displacement boundary is hinged support. In this section, the calculation methods of ocean environment load, contact force between riser and test pipe, impact load of high-speed fluid in pipe and heave motion equation of platform will be established.

2.2.1 Ocean environment load (load boundary condition)

It is assumed that the relative velocity between the fluid and the riser is V_r, and the outflow velocity of the riser is U_c. For steady flow, the steady-state drag force and lift force acting on the riser are shown in Fig. 3.

According to Morison's equation, the steady-state drag and lift forces acting on the riser are written as:

$$\begin{cases} \overline{F}_D = \dfrac{1}{2}\rho_w V_r^2 D_o \overline{C}_d \\ \overline{F}_L = \dfrac{1}{2}\rho_w V_r^2 D_o \overline{C}_l \end{cases} \tag{16}$$

where $\overline{C}_d$ is the coefficient of steady-state drag force; $\overline{C}_l$ is coefficient of steady lift force; and ρ_w is seawater density (kg/m^3).

The components of fluid force acting on the riser in the IL direction and CF direction can be expressed as follows:

$$\begin{cases} F'_x = \dfrac{1}{2}\rho_w V_r^2 D_o \left(\overline{C}_d \cos\theta + \overline{C}_l \sin\theta \right) \\ F'_y = \dfrac{1}{2}\rho_w V_r^2 D_o \left(-\overline{C}_d \sin\theta + \overline{C}_l \cos\theta \right) \end{cases} \tag{17}$$

Given that

$$\begin{cases} \theta = \tan^{-1}\left[\dfrac{\partial v_y}{\partial t} \Big/ \left(U_c - \dfrac{\partial v_x}{\partial t} \right) \right] \\ V_r = \sqrt{\left(\dfrac{\partial v_y}{\partial t} \right)^2 + \left(U_c - \dfrac{\partial v_x}{\partial t} \right)^2} \end{cases} \tag{18}$$

The components of fluid force can be written further as:

$$\begin{cases} F'_x = \dfrac{1}{2}\rho_w U_c D_o \left[\overline{C}_d \left(V_r - \dfrac{V_r}{U_c} \dfrac{\partial v_x}{\partial t} \right) + \overline{C}_l \dfrac{V_r}{U_c} \dfrac{\partial v_y}{\partial t} \right] \\ F'_y = \dfrac{1}{2}\rho_w U_c D_o \left[\overline{C}_l \left(V_r - \dfrac{V_r}{U} \dfrac{\partial v_x}{\partial t} \right) - \overline{C}_d \dfrac{V_r}{U_c} \dfrac{\partial v_y}{\partial t} \right] \end{cases} \tag{19}$$

In addition to the steady-state component, the fluid force acting on the riser also includes harmonic pulsating drag force and pulsating lift force.

$$\begin{cases} F'_D = \dfrac{1}{2}\rho_w U_c^2 D_o C_D \\ F'_L = \dfrac{1}{2}\rho_w U_c^2 D_o C_L \end{cases} \tag{20}$$

where F'_D, C_D are the fluctuating drag force and corresponding coefficient, respectively; F'_L, C_L are fluctuating lift force and corresponding coefficient, respectively.

Therefore, according to Eqs. (19) and (20), all fluid forces acting on the riser can be written as:

$$\begin{cases} F_D(z,t) = F_x + F'_D = \dfrac{1}{2}\rho_w U_c D_o \left[\overline{C}_d \left(V_r - \dfrac{V_r}{U_c} \dfrac{\partial v_x}{\partial t} \right) + \overline{C}_l \dfrac{V_r}{U_c} \dfrac{\partial v_y}{\partial t} \right] \\ \quad + \dfrac{1}{2}\rho_w U_c^2 D_o C_D \\ F_L(z,t) = F_y + F'_L = \dfrac{1}{2}\rho_w U_c D_o \left[\overline{C}_l \left(V_r - \dfrac{V_r}{U} \dfrac{\partial v_x}{\partial t} \right) - \overline{C}_d \dfrac{V_r}{U_c} \dfrac{\partial v_y}{\partial t} \right] \\ \quad + \dfrac{1}{2}\rho_w U_c^2 D_o C_L \end{cases} \tag{21}$$

It is noted that the steady-state lift coefficient $\overline{C}_l$ is taken as 0 for the circular section and $V_r \approx U_c - \partial v_x/\partial t$. Ignoring the effect of higher-order terms, fluid forces can be further written as

$$\begin{cases} F_D(z,t) = \dfrac{1}{2}\rho_w U_c^2 D_o \overline{C}_d - \rho_w U_c D_o \overline{C}_d \dfrac{\partial v_x}{\partial t} + \dfrac{1}{2}\rho_w U_c^2 D_o C_D \\ F_L(z,t) = -\dfrac{1}{2}\rho_w U_c D_o \overline{C}_d \dfrac{\partial v_y}{\partial t} + \dfrac{1}{2}\rho_w U_c^2 D_o C_L \end{cases} \tag{22}$$

In this paper, the van der Pol nonlinear vibration equation is used to describe the shedding characteristics of fluid vortex. According to the discussion on the coupling term of the wake vibrator by [5], when the coupling term is acceleration, the calculation results are more consistent with the experimental results. Therefore, the governing equation of the wake
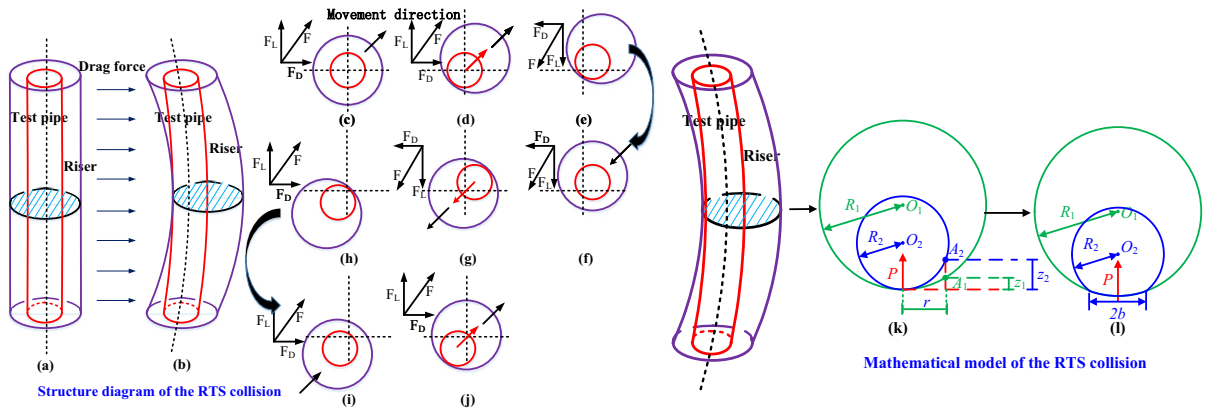
Fig. 4 Contact deformation between the riser and test pipe
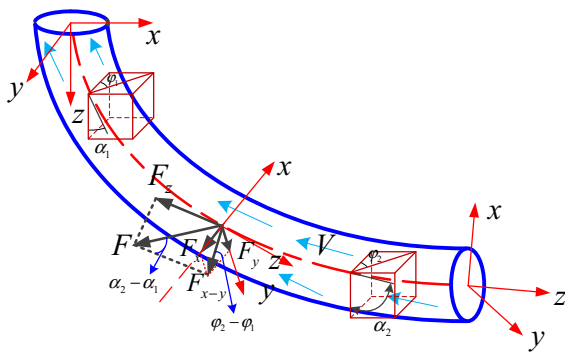

Fig. 5 Schematic of the impact load by high-speed gas

oscillator model based on acceleration coupling is used as follows:

$$\begin{cases} \ddot{q}_x + \varepsilon_x \omega'_s (q_x^2 - 1) \dot{q}_x + (2\omega'_s)^2 q_x = \dfrac{A_x}{D_i} \ddot{v}_x \\ \ddot{q}_y + \varepsilon_y \omega'_s (q_y^2 - 1) \dot{q}_y + (\omega'_s)^2 q_y = \dfrac{A_y}{D_i} \ddot{v}_y \end{cases} \quad (23)$$

where q_x and q_y are the dimensionless wake oscillator variables in IL and CF directions, respectively; $\omega'_s (= 2\pi S_t |U_c - \dot{v}_x| / D_o)$ is the vortex shedding frequency(S_t is Strouhal number); and ε_x, ε_y, A_x, A_y are dimensionless parameters determined by experiment.

The fluctuating drag force coefficient C_D and the fluctuating lift force coefficient C_L are expressed by the dimensionless wake oscillator variables q_x and q_y, respectively, namely

$$C_D = C'_d \frac{q_x}{2}, \quad C_L = C'_l \frac{q_y}{2} \quad (24)$$

Substituting Eq. (24) into Eq. (22), the final form of external flow force acting on the riser can be obtained as

$$\begin{cases} F_D(z,t) = \dfrac{1}{2}\rho_w U_c^2 D_o \overline{C}_d - \rho_w U_c D_o \overline{C}_d \dfrac{\partial v_x}{\partial t} + \dfrac{1}{2}\rho_w U_c^2 D_o C'_d \dfrac{q_x}{2} \\ F_L(z,t) = -\dfrac{1}{2}\rho_w U_c D_o \overline{C}_d \dfrac{\partial v_y}{\partial t} + \dfrac{1}{2}\rho_w U_c^2 D_o C'_l \dfrac{q_y}{2} \end{cases} \quad (25)$$

In this study, $A_x = 48, A_y = 12, \varepsilon_x = 1.2, \varepsilon_y = 0.3$, $C'_d = 0.3, C'_l = 0.4$, according to [5], and [48].

2.2.2 Nonlinear contact/collision load between the riser–test pipe (load boundary condition)

A method for calculating the riser–test pipe contact/collision load has been established according to the elastoplastic mechanics theory [47]. The deformation structure is illustrated in Fig. 4. The relation between contact/impact load and deformation and the friction of RTS can be obtained, whose detailed derivation is demonstrated in our recent work [39].

$$\begin{cases} \delta = 1.82 \dfrac{F}{E} \left[1 - \ln\left(1.522 \sqrt{\dfrac{F}{\pi} \dfrac{R_1 R_2}{R_2 - R_1}} \right) \right] \\ f_F = \xi F \end{cases} \quad (26)$$

where δ is the relative deformation between riser and test pipe (m); f_F is the friction of RTS (N); F is contact load of riser–test pipe (N); E is the elastic modulus of the riser or test pipe material (Pa); R_1 and R_2 are the radius of riser and test pipe, respectively (m); and ξ is the friction coefficient between the riser and test pipe,

which can be determined using the method proposed by Wen et al. [49] or by performing a wear test. In our present study, a wear test revealed that the friction coefficient is 0.243 for the gas wells in the South China Sea [50].

2.2.3 High-speed fluid impact load in test pipe (load boundary condition)

In the testing condition, when the high-speed fluid in the test pipe passes through regions with changing well inclination angles or deformation area, it generates an impact load on the test pipe (as shown in Fig. 5), resulting in longitudinal and lateral vibrations of the test pipe. According to fluid mechanics [51], the high-speed fluid impact load in the test pipe can be calculated using the following equations:

$$
\begin{cases}
f_x(x,t) = -\rho_i A_i V^2 \sin[\alpha_2(t) - \alpha_1(t)] \cos[\varphi_2(t) - \varphi_1(t)] \\
f_y(x,t) = -\rho_i A_i V^2 \sin[\alpha_2(t) - \alpha_1(t)] \sin[\varphi_2(t) - \varphi_1(t)] \\
f_z(x,t) = -\rho_i A_i V^2 \cos[\alpha_2(t) - \alpha_1(t)]
\end{cases}
\tag{27}
$$

where ρ_i is the density of gas in the test pipe (kg/m³); A_i is the cross-sectional area of the wellbore (m²); and $\alpha_1(t)$, $\alpha_2(t)$, $\varphi_1(t)$ and $\varphi_2(t)$ are, respectively, the deflection angles of the upper and lower micro-segments of the test pipe in x- and y-directions (rad), which are determined by the inclination angle and the deformation of the test pipe.

Meanwhile, the inclination angle and azimuth at any depth can be determined through the cubic spline interpolation method [52], which can be expressed as follows in the interval $[s_{k-1}, s_k]$ $(k = 1, 2, \ldots, N)$:

$$
\begin{cases}
\alpha(s) = \dfrac{M_{k-1}(s_k - s)^3}{6L_k} + \dfrac{M_k(s - s_{k-1})^3}{6L_k} + C_k(s - s_{k-1}) + C_{k-1}(s_k - s) \\
\varphi(s) = \dfrac{m_{k-1}(s_k - s)^3}{6L_k} + \dfrac{m_k(s - s_{k-1})^3}{6L_k} + c_k(s - s_{k-1}) + c_{k-1}(s_k - s)
\end{cases}
\tag{28}
$$

where $C_j = \frac{\alpha_j}{L_k} - \frac{M_j L_k}{6}, j = k, k - 1$; $c_j = \frac{\varphi_j}{L_k} - \frac{m_j L_k}{6}, j = k, k - 1$; $M_j = \alpha_j'', j = k, k - 1$; $m_j = \varphi_j'', j = k, k - 1$; k is the order number of measuring point; $L_k = s_k - s_{k-1}$ is the length of measuring section (m); s is the well depth at the measuring point (m); and N is the total measuring point.

2.2.4 Displacement boundary condition

The different working conditions and the different riser hang-off conditions are mainly different in the upper and lower boundary conditions. In the testing condition, as shown in Fig. 2, the upper end of the riser is connected to the platform with flexible joint (the rotational stiffness of the upper flexible joint is K_U (N·m/deg), which can be determined in Mao's recent work [53], and the RTS can move with the movement of the platform. In this study, the heave motion of the platform is mainly considered and the influence of horizontal motion is ignored. That is to say, the horizontal displacement of the platform is 0. The lower end of the RTS is connected to the BOP, and the rotational stiffness is K_L (N·m/deg), which also can be determined in Mao's recent work. Therefore, the displacement boundary and initial conditions of the RTS under the normal drilling condition can be expressed as:

For the riser:

$$
\begin{cases}
v_x(0,t) = 0, v_y(0,t) = 0, v_z(0,t) = u_{\text{boat}}(t), v_x(L,t) = 0, v_y(L,t) = 0, v_z(L,t) = 0 \\
EI_v v_x''|_{(0,t)} = K_U v_x'|_{(0,t)}, EI_v v_y''|_{(0,t)} = K_U v_y'|_{(0,t)}, EI_v v_x''|_{(L,t)} = K_L v_x'|_{(L,t)}, EI_v v_y''|_{(L,t)} = K_L v_y'|_{(L,t)} \\
v_x(z,0) = 0, v_y(z,0) = 0, v_z(z,0) = 0, v_x'|_{(z,0)} = 0, v_y'|_{(z,0)} = 0, EI v_x''|_{(z,0)} = 0, EI v_y''|_{(z,0)} = 0
\end{cases}
\tag{29}
$$

For the test pipe:

$$
\begin{cases}
S_x(0,t) = 0, S_y(0,t) = 0, S_z(0,t) = u_{\text{boat}}(t), S_x(L,t) = 0, S_y(L,t) = 0, S_z(L,t) = 0 \\
EI_s S_x''\big|_{(0,t)} = K_U S_x'\big|_{(0,t)}, EI_s S_y''\big|_{(0,t)} = K_U S_y'\big|_{(0,t)}, EI_s S_x''\big|_{(L,t)} = K_L S_x'\big|_{(L,t)}, EI_s S_y''\big|_{(L,t)} = K_L S_y'\big|_{(L,t)} \\
S_x(z,0) = 0, S_y(z,0) = 0, S_z(z,0) = 0, EIS_x'\big|_{(z,0)} = 0, EIS_y'\big|_{(z,0)} = 0, EIS_x''\big|_{(z,0)} = 0, EIS_y''\big|_{(z,0)} = 0
\end{cases}
\tag{30}
$$

where $u_{\text{boat}}(t)$ is the heave displacement of the platform (m).

2.2.5 Heave motion equation of platform

In the deepwater test condition, it is necessary to establish the heave motion model of the platform under the action of random waves to determine the upper boundary displacement of the RTS. According to Shen's work [54], the heave motion equation of platform can be expressed as follows:

$$
\begin{aligned}
m_p \ddot{u}_{\text{boat}} &+ B_1 \dot{u}_{\text{boat}} + B_2 \dot{u}_{\text{boat}} |\dot{u}_{\text{boat}}| \\
&+ \rho_w g A_w (u_{\text{boat}} - \eta(t)) \\
&= \overline{F}_z
\end{aligned}
\tag{31}
$$

where m_p is the mass of platform (m); B_1 and B_2 are heave radiation and heave viscous damping; A_w is the area of the platform at sea level (m^2); and $\eta(t)$ and $\overline{F}_z$ are the surface displacement of random wave (m) and random heave wave exciting force on platform (N).

In this study, the random wave surface displacement can be determined using Longuet-Higgins model [55], which can be expressed as follows:

$$
\eta(t) = \sum_{i=1}^{M} a_i \cos[\hat{\omega}_i t + \varepsilon_i]
\tag{32}
$$

where $\hat{\omega}_i (= (\omega_{i-1} - \omega_i)/2)$ is circular frequency of the i th harmonic (Hz); ε_i is the initial phase of the i th harmonic component (rad), taking the random number in the range $(0, 2\pi)$; M is the interval number of partition; $a_i (= \sqrt{2S(\omega)\Delta\omega})$ is amplitude of the i th harmonic component (m); $\Delta\omega (= (\omega_H - \omega_L)/N)$ is the frequency step; and $S(\omega)$ is the random wave spectrum, which was described using JONSWAP

spectrum in this study. The expression can be obtained in the Shen's work [54]:

$$
\begin{cases}
S(\omega) = \dfrac{0.06238(1.094 - 0.01915 \ln \gamma)}{0.23 + 0.0336\gamma - 0.185(1.9 + \gamma)^{-1}} \\
\quad H_{1/3}^2 T_P^{-4} f^{-5} \exp\left[-\dfrac{5}{4}(T_P f)^{-4}\right] \gamma^{\exp\left[-(f/f_p - 1)^2/2\sigma^2\right]} \\
T_p = \dfrac{T_{1/3}}{1 - 0.132(\gamma + 0.2)^{-0.559}}, \ \sigma = \begin{cases} 0.07, & f \leq f_p \\ 0.09, & f > f_p \end{cases}
\end{cases}
\tag{33}
$$

where f is the frequency (Hz), and ω is the circular frequency (Hz), $\omega = 2\pi f$; $H_{1/3}$ and $T_{1/3}$ are the significant wave height (m) and significant period (s) of the wave; f_p and T_p are peak frequency (Hz) and peak period (s) of the wave; γ is peak parameters, which is 3.3 in this study; and σ is the peak shape coefficient.

Also, according to Shen's work [54], the random heave wave exciting force on platform includes two parts: One is the exciting force of the random wave on the platform body ($F_s(t)$), and the other is the exciting force of the random wave on the heave plate ($F_p(t)$), which can be expressed as follows:

$$
\begin{aligned}
\overline{F}_z &= F_s(t) + F_p(t) \\
&= 2\rho_w g \pi R^2 \left[1 - \frac{1}{2}\sin(kR)\right]\left(\frac{J_1(kR)}{kR}\right)e^{-kd}\eta(t) \\
&\quad + 0.597\frac{\rho_w g}{4}\omega^2 e^{k z_{\text{plate}}} B_{\text{plate}}^3 \eta(t)
\end{aligned}
\tag{34}
$$

where R is platform radius (m); k is wave number; $J_1(\cdot)$ is the first-order Bessel function of first kind; d is the draft of platform (m); z_{plate} is the depth of heave plate (m); and B_{plate} is the width of heave plate (m).
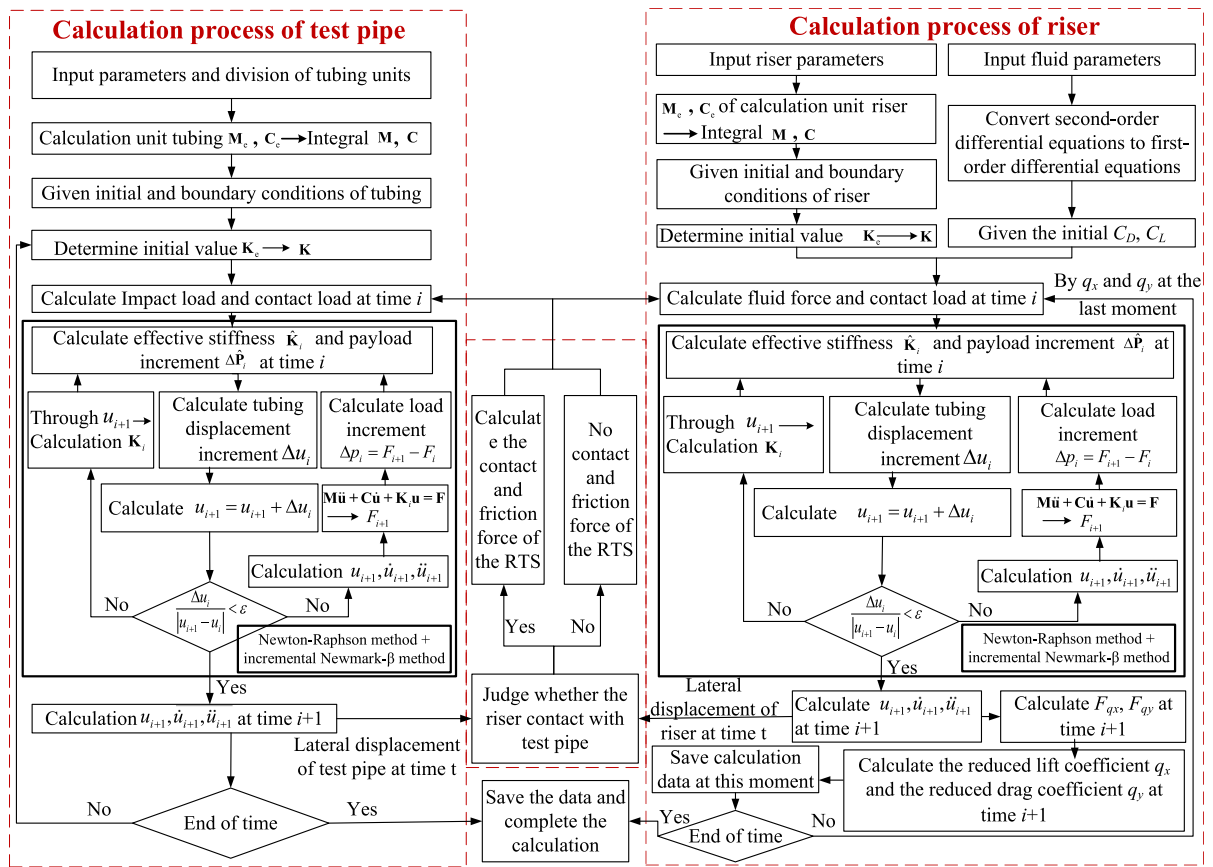
Fig. 6 Flowchart of solving nonlinear vibration model of the RTS

2.3 Solution scheme

This study used the linear Lagrange and cubic Hermitian functions (micro-finite method) to express the longitudinal/transverse displacements of riser and test pipe; the finite element discrete forms can be expressed as follows:

$$
\begin{cases}
\upsilon_x = \varphi_x^{\mathbf{T}}\mathbf{d} & \upsilon_y = \varphi_y^{\mathbf{T}}\mathbf{d} & \upsilon_z = \varphi_z^{\mathbf{T}}\mathbf{d} \\
S_x = \varphi_x^{\mathbf{T}}\overline{\mathbf{d}} & S_y = \varphi_y^{\mathbf{T}}\overline{\mathbf{d}} & S_z = \varphi_z^{\mathbf{T}}\overline{\mathbf{d}}
\end{cases}
\tag{35}
$$

where $\mathbf{d}$ and $\overline{\mathbf{d}}$ are the displacement vectors of riser and test pipe unit, respectively; φ_x, φ_y and φ_z, respectively, represent the vibration shape function of riser and test pipe unit, which are expressed as:

$$
\begin{bmatrix} \dfrac{\mathbf{d}}{\mathbf{d}} \\ \varphi_x \\ \varphi_y \\ \varphi_z \end{bmatrix}^{\mathbf{T}} = \left(\begin{bmatrix} \upsilon_{z1} \\ \upsilon_{x1} \\ \dfrac{d\upsilon_{x1}}{dz} \\ \upsilon_{y1} \\ \dfrac{d\upsilon_{y1}}{dz} \\ \upsilon_{z2} \\ \upsilon_{x2} \\ \dfrac{d\upsilon_{x2}}{dz} \\ \upsilon_{y2} \\ \dfrac{d\upsilon_{y2}}{dz} \end{bmatrix}, \begin{bmatrix} S_{z1} \\ S_{x1} \\ \dfrac{dS_{x1}}{dz} \\ S_{y1} \\ \dfrac{dS_{y1}}{dz} \\ S_{z2} \\ S_{x2} \\ \dfrac{dS_{x2}}{dz} \\ S_{y2} \\ \dfrac{dS_{y2}}{dz} \end{bmatrix}, \begin{bmatrix} 0 \\ 1-\dfrac{3z^2}{l^2}+\dfrac{2z^3}{l^3} \\ z-\dfrac{2z^2}{l}+\dfrac{z^3}{l^2} \\ 0 \\ 0 \\ 0 \\ \dfrac{3z^2}{l^2}-\dfrac{2z^3}{l^3} \\ -\dfrac{z^2}{l}+\dfrac{z^3}{l^2} \\ 0 \\ 0 \end{bmatrix}, \begin{bmatrix} 0 \\ 0 \\ 0 \\ 1-\dfrac{3z^2}{l^2}+\dfrac{2z^3}{l^3} \\ z-\dfrac{2z^2}{l}+\dfrac{z^3}{l^2} \\ 0 \\ 0 \\ 0 \\ \dfrac{3z^2}{l^2}-\dfrac{2z^3}{l^3} \\ -\dfrac{z^2}{l}+\dfrac{z^3}{l^2} \end{bmatrix}, \begin{bmatrix} 1-\dfrac{z}{l} \\ 0 \\ 0 \\ 0 \\ 0 \\ \dfrac{z}{l} \\ 0 \\ 0 \\ 0 \\ 0 \end{bmatrix} \right) \tag{36}
$$

By substituting the displacement obtained from Eqs. (35) and (36) into the energy functional of the RTS, the standard forms of the strain energy function U, kinetic energy function T and energy function with external force W expressed by the node displacement vectors can be obtained. After assembling the structural elements, the discrete dynamic equation of the system can be obtained according to the variational principle:

$$\mathbf{M}(t)\ddot{\mathbf{D}} + \mathbf{C}(t)\dot{\mathbf{D}} + \mathbf{K}(t)\mathbf{D} = \mathbf{F}(t) \tag{37}$$

where $\mathbf{D}$ represents the matrix of overall displacement, which is given by Eq. (35); $\mathbf{F}(t)$ represents the load column vector of the structure, which accounts for the impact force of gas on the test pipe as well as the contact/friction force of the tubing–casing, ocean environment load and the expressions of them shown in Sect. 2.2; and $\mathbf{K}(t)$, $\mathbf{M}(t)$ and $\mathbf{C}(t)$ represent the matrices of the overall stiffness, mass and damping, respectively.

Because there are too many nonlinear factors considered in the 3D nonlinear vibration model, the calculation accuracy of model will be decreased and the model will be difficult to converge if only using Newmark-β method for gradual integration. Therefore, in this study, the incremental Newmark-β method and Newton–Raphson method are used to solve the discrete Eq. (37) simultaneously, and the specific derivation process can be seen in our previous work [56]. The wake vibrator (shown in Eq. (23)) is

Table 1 Simulated experiment parameters

Parameter	Test pipe outer diameter (m)	Test pipe inner diameter (m)	Test pipe length (m)	Riser outer diameter (m)	Riser inner diameter (m)	Gas flow velocity (m/s)	Elastic modulus (GPa)	Density (kg/m³)	External velocity (m/s)
Actual parameter	0.1143	0.095	579.7	0.2445	0.2168	18.05	206.0	7850	0.5
Test parameter	0.016	0.014	3.0	0.034	0.030	18.05	3.92	1150	0.5

(a)

(b) Diagram of experimental pool

(c) Structure diagram of test bench

(d) Schematic of upper and lower boundary joints
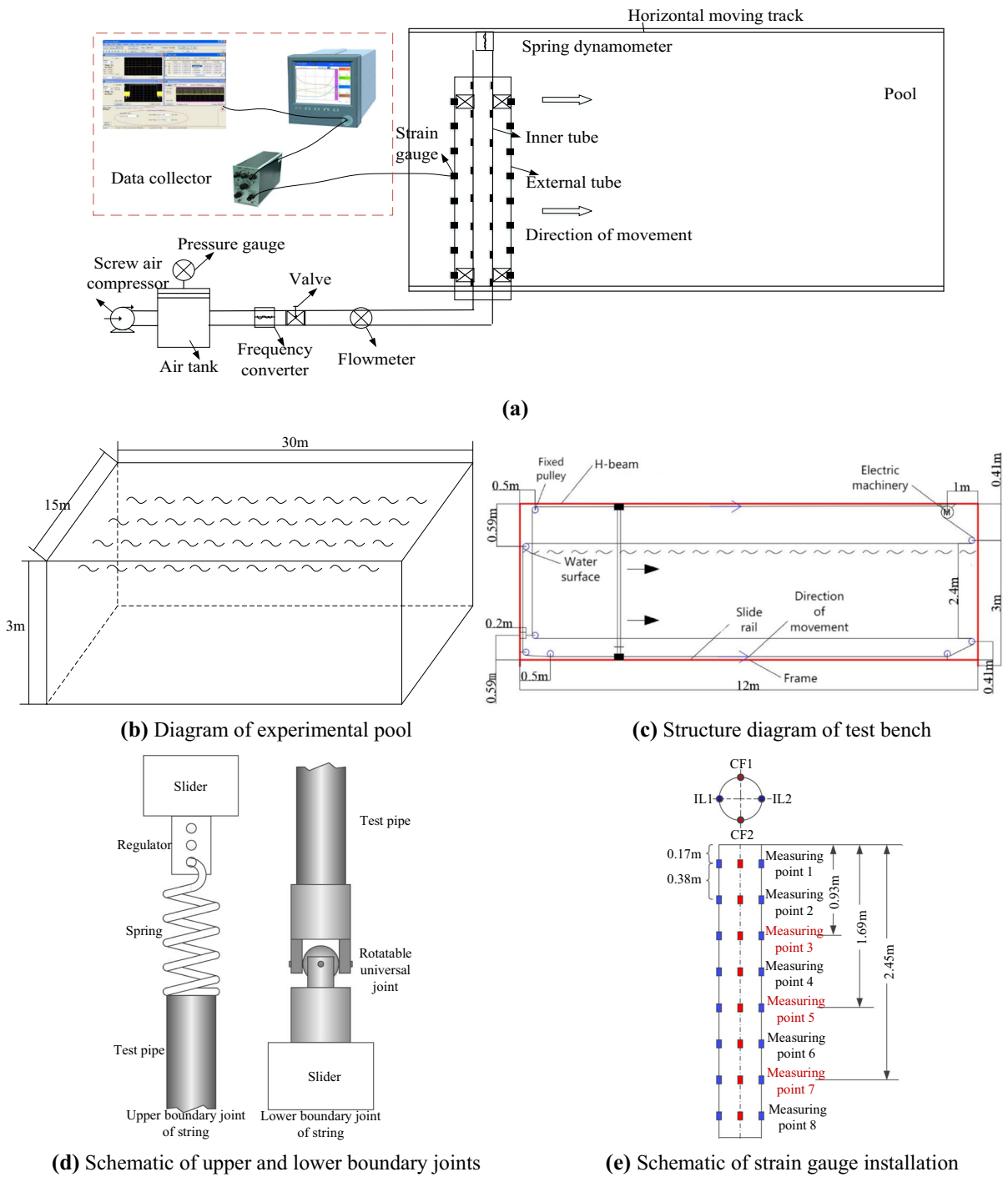

(e) Schematic of strain gauge installation
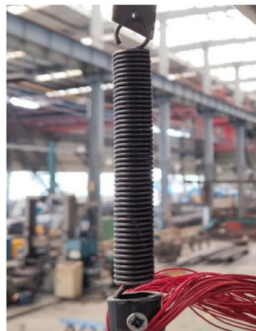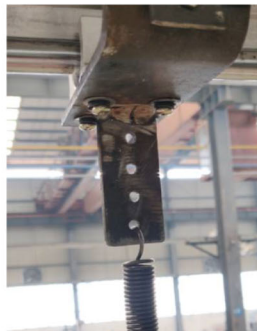
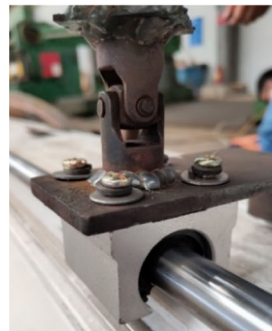**Fig. 7** Experimental system design

(a) Physical drawing of test bench

(b) Adjusting spring **(c)** Tension adjustment device **(d)** Bottom universal joint **(e)** Gas transportation system

(f) Experimental pool

Fig. 8 Physical diagram of test system

solved by a fourth-order Runge–Kutta technique [22]. The coupling iteration between the Runge–Kutta technique and incremental Newmark-β method was performed to determine the dynamic response of the RTS. The solution flow of the nonlinear dynamic model is shown in Fig. 6, and its FORTRAN calculation code was developed.

2.4 Experimental verification

2.4.1 Simulated experimental parameters

Because the vibration data of deepwater RTS cannot be accurately measured onsite, a simulation experiment is performed to validate the nonlinear vibration model in this study. Three criteria should be satisfied for the similarity experiment of RTS vibration: geometric similarity, motion similarity and dynamic similarity [57, 58]. Based on field parameters of BY-M

(a) The RMS of riser in IL direction

(b) The RMS of riser in CF direction
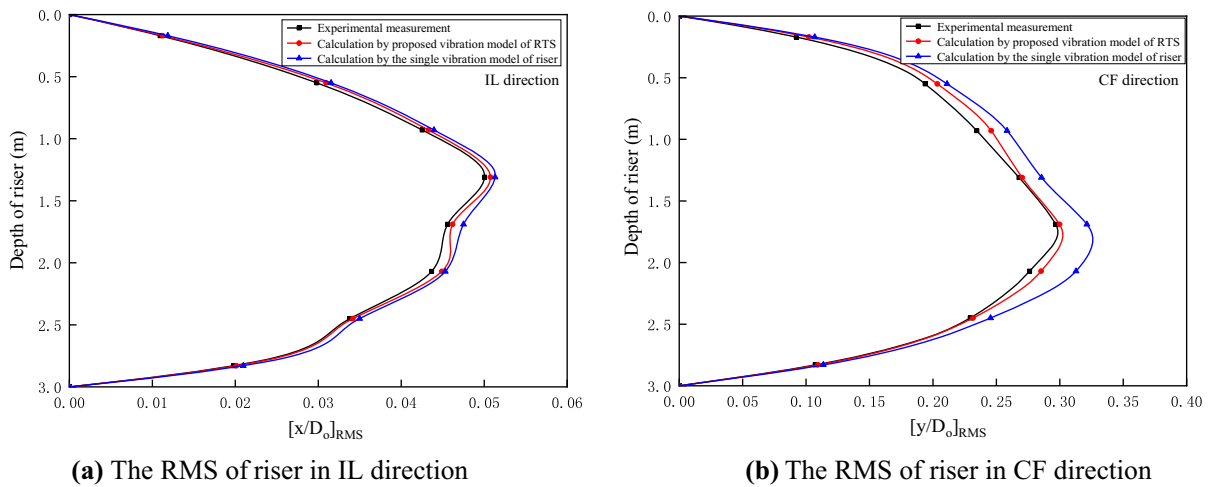
Fig. 9 The RMS distribution of riser displacement

(a) The amplitude frequency response curve of riser in IL direction

(b) The amplitude frequency response curve of riser in CF direction
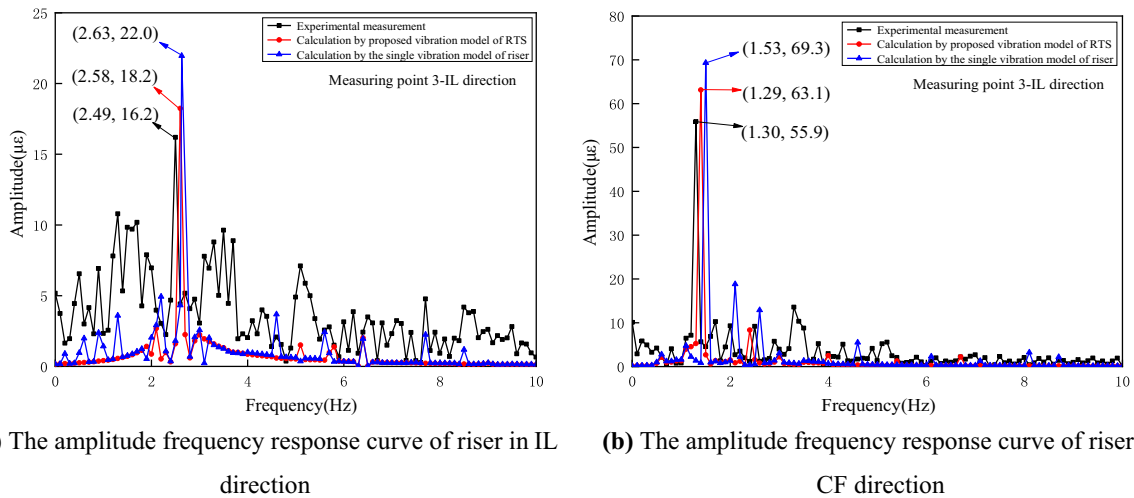
Fig. 10 The amplitude–frequency response curve of riser at measuring point 3

gas well in deepwater block of South China Sea and simulation experiment area conditions, the basic sizes of the riser and test pipe (inner diameter, outer diameter, tube length, etc.) in the simulation experiment are determined using geometric similarity. Because the size difference between the length and radial directions is considerable, the uniform scale ratio is not adopted. The similarity ratios in the radial and length directions are set as 7.14 and 193.2, respectively. According to our recent work [39], the material density and elastic modulus of the experimental pipe string and the actual pipe string should satisfy the following:

$$\frac{E_p/E_m}{\rho_p/\rho_m} = \lambda = 7.14 \tag{38}$$

where ρ_p and E_p represent the density (kg/m^3) and elastic modulus (Pa) of the actual RTS, respectively; ρ_m and E_m represent the density (kg/m^3) and elastic modulus (Pa) of the RTS in the simulation experiment, respectively; and λ represents the principal similarity ratio (radial similarity ratio). Thus, by substituting the density ($\rho_p = 7850$ kg/m^3) and elastic modulus ($E_p = 206$ GPa) of the actual RTS into Eq. (38), we obtain the following:

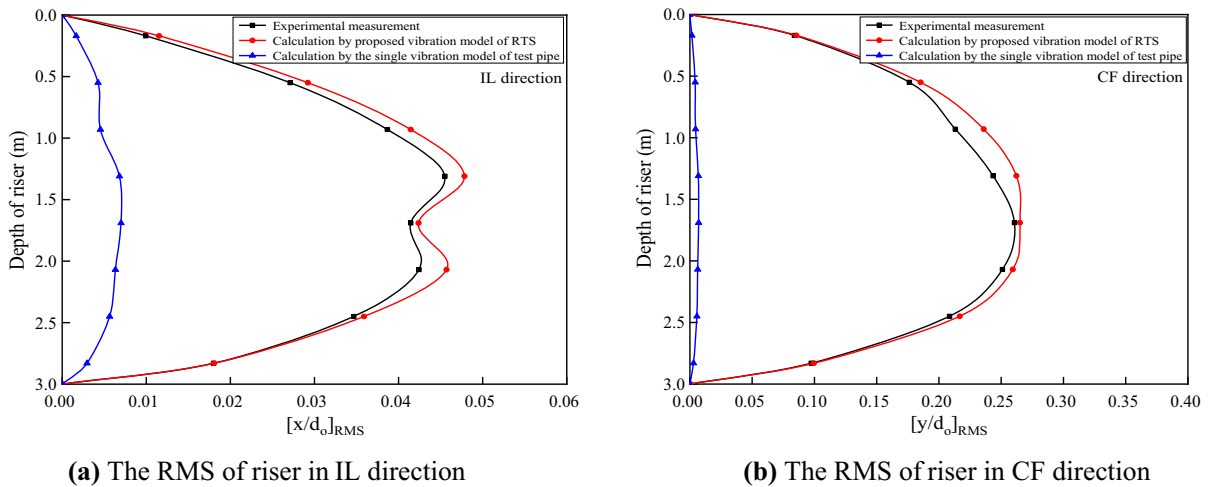**(a)** The RMS of riser in IL direction

(b) The RMS of riser in CF direction

Fig. 11 The RMS distribution of test pipe displacement

(a) The amplitude frequency response curve of test pipe in IL direction

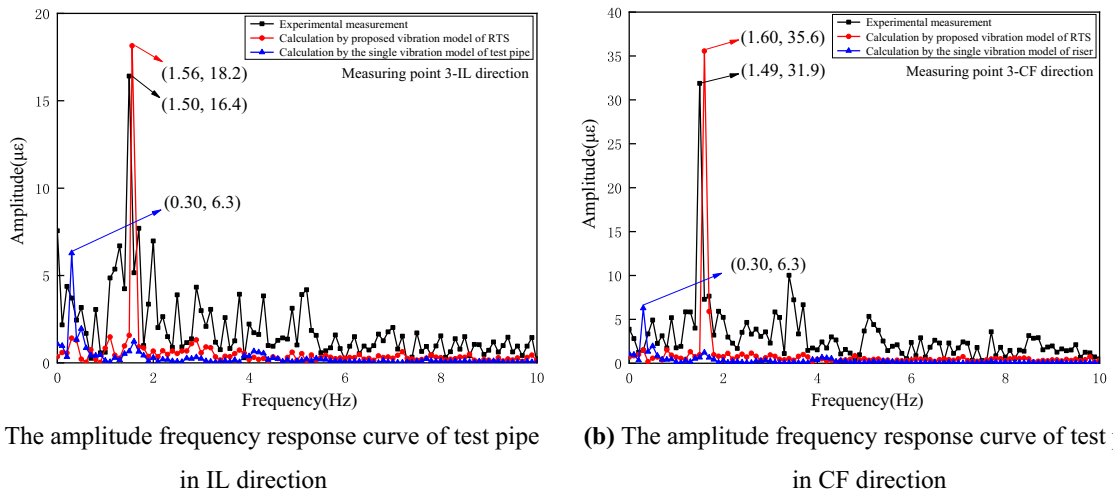**(b)** The amplitude frequency response curve of test pipe in CF direction

Fig. 12 The amplitude–frequency response curve of test pipe at measuring point 3

$$\frac{E_m}{\rho_m} = \frac{1}{7.14}\frac{E_p}{\rho_p} \approx 3.68 \times 10^{-3}\text{GPa} \cdot \left(\frac{\text{kg}}{\text{m}^3}\right)^{-1} \quad (39)$$

According to the elastic modulus/density ratio, the PVC tube is selected to satisfy the requirement by referring to the metal materials manual [59]. Its elastic modulus and density are $E_m = 3.92$ GPa and $\rho_m = 1150$ kg/m³, respectively.

According to the dynamic similarity, the fluid velocity of the simulated experiment is consistent with the actual fluid velocity onsite. Thus, we can obtain the experimental gas flow, which is 239.95 m³/d, and the rated pressure, motor power and maximum flow of the air compressor are 1.25 MPa, 2200 W and 302.4 m³/
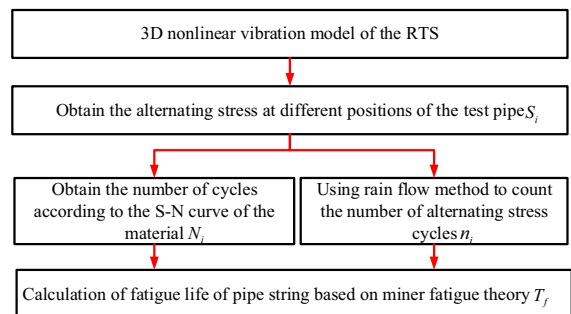
Fig. 13 Flowchart of fatigue life analysis of test pipe

d, respectively, which can satisfy the requirements of the simulation experiment (as shown in Fig. 8e). To accurately determine the vibration amplitude and frequency of the pipe, strain gauges are used to measure the strain characteristics at different locations of the pipe. All parameters of the final simulation experiment are shown in Table 1.

2.4.2 Simulation experimental system

The experimental system is mainly composed of experimental pool, experimental bench, string system, data testing system and gas supply system (as shown in Fig. 7a). The size of experimental pool is 30 m × 15 m × 3 m (as shown in Fig. 7b). The experimental bench is mainly composed of experimental steel frame, which is welded by H-beam (12.5 m long and 3.5 m high), poplar roller, fixed pulley, wire rope, track, etc. (as shown in Fig. 7c). Its function is to change the movement direction of the wire rope using the fixed pulley, so as to ensure that the movement direction and speed of the top and bottom wire ropes are consistent. Meanwhile, using the wire rope to drag the experimental string can realize the synchronous movement of the string, so as to ensure the force of the simulated uniform current. The experimental string system consists of inner and outer simulated tubes and upper and lower joint simulators, in which the upper end of the string is connected with the slider by a spring with elastic stiffness, and the lower end is connected with the lower slider by a rotatable universal joint (as shown in Fig. 7d). The data test system consists of strain gauge, shield wire and data acquisition instrument, in which the measurement accuracy and sampling frequency of the strain gauges are 7.5 με and 500 Hz,, respectively. As

shown in Fig. 7e, eight measurement points are arranged around the pipe, for a total of 32 points. Nodes 1 and 8 are 0.17 m from the ends of the pipe, and eight measurement points are evenly arranged along the length direction of the pipe at intervals of 0.38 m. The gas supply and transportation system consists of screw air compressor, high-pressure gas storage tank, connecting pipeline, flowmeter, solenoid valve, etc. The physical diagrams of each part of the experimental system are shown in Fig. 8.

2.4.3 Experimental results

In the experiment, eight measuring points are arranged on the surface of the inner and outer pipe. Four groups of strain gauges are arranged on the section of the same measuring point, which are uniformly distributed 90° along the circumference of the pipe. The vibration characteristics of the pipe in the flow direction are measured by in-line flow 1 (IL1) and in-line flow 2 (IL2), and those in the vertical flow direction are measured by cross-flow 1 (CF1) and cross-flow 2 (CF2), as shown in Fig. 7e. According to the theoretical model established in the first section, the single riser vibration model [22] and the single flow-induced vibration model of the test pipe [39] in our recent researches, the vibration response of the RTS is calculated using the same parameters as the test parameters (as shown in Table 1), in which the riser and test pipe were divided into 300 units. The simulation time is 10 s, and the step size is 0.001 s.

Figures 9 and 10 show the root-mean-square (RMS) distribution and the amplitude–frequency response curve (at the measuring point 3) of the riser displacement in IL and CF direction. It can be seen from Fig. 9 that the CF RMS of the riser is
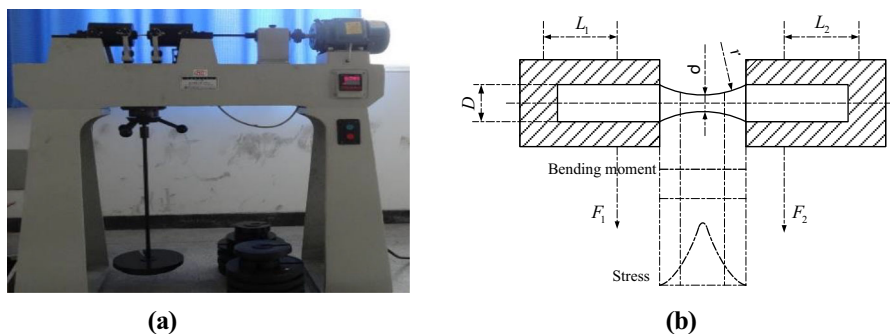

Fig. 14 PQ-6 pure bending fatigue testing machine (**a**) and stress analysis diagram of test specimen (**b**)
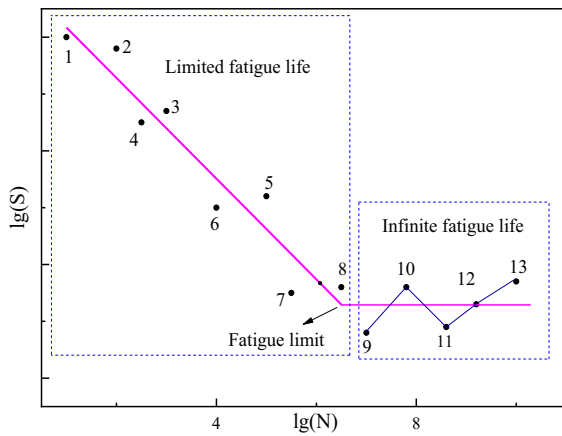
Fig. 15 Schematic diagram of measuring S–N curve

Table 3 Test data of infinite fatigue limit zone

Number	Stress (MPa)	Cycle times	Result
1	385	10,654,984	Suspension
2	405	10,343,146	Suspension
3	425	323,889	Invalid
4	405	10,153,919	Suspension
5	425	307,439	Invalid
6	405	3,245,607	Invalid
7	385	10,438,520	Suspension
8	405	1,018,500	Invalid
9	385	10,248,537	Suspension

Table 2 Test data of limited fatigue life zone

Stress amplitude S (MPa)	Cycle times N	The logarithmic form of the number of cycles (lgN)	Logarithmic form of stress (lgS)
585	14,611	4.16	2.77
535	42,749	4.63	2.73
485	79,520	4.90	2.68
435	258,661	5.41	2.63
425	289,239	5.46	2.62
415	540,381	5.73	2.61
405	7,914,224	6.79	2.60

significantly greater than the IL RMS. Through the comparison of the experimental data, the calculation results using the proposed model in Sect. 2.1 and the single riser model in our recent work [22], it is found that the calculation results of the proposed model are closer to the experimental data, which verified the correctness and effectiveness of the proposed model. It can be discovered in Fig. 10 that, regardless of the experimental results and the theoretical calculation results, the IL vibration frequency of the riser was twice that of the CF vibration frequency, which was consistent with the previous research results [11, 22]. The amplitude of the riser using the single vibration model is the largest, and the main reason is that there is no restraining effect of the test pipe. By observing the experimental amplitude–frequency response of the measurement point 3, it is found that the vibration was obviously complex, which is mainly affected by the external factors in the test process. Meanwhile, compared with calculation results using the single vibration model, the calculation results in this paper

are closer to the experimental results, which verifies the correctness of the RTS vibration model again.

Figures 11 and 12 show the RMS distribution and the amplitude–frequency response curve (at the measuring point 3) of the test pipe displacement in IL and CF direction. It can be noted in Fig. 11 that when the riser is fixed and only the flow-induced vibration (FIV) of the test pipe is considered, the calculated results of test pipe are significantly smaller than the experimental results and the calculation results in this paper, which indicates that the vibration of the test pipe was mainly caused by the riser vibration. Therefore, the nonlinear vibration of the riser cannot be ignored in the vibration analysis of the test pipe, and the calculation results of test pipe obtained using the proposed nonlinear model of RTS can be closer to reality. It can be observed in Fig. 12 that the main frequency obtained by the single test pipe vibration model is significantly lower than that of the test and the calculation results of proposed model. It shows again that the influence of riser should be considered when

Table 4 Load-type correction factor C_L [62]

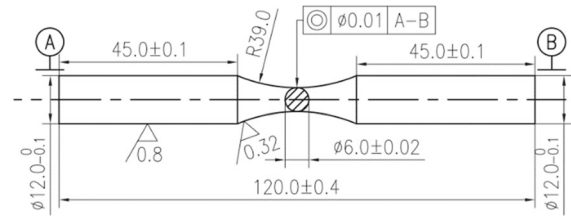| Loading type	Pure bending load	Axial load (slightly bent)	Reverse about steel	Reverse about cast iron
C_L	0.9	0.7	0.58	0.8

Fig. 16 Dimension drawing of test specimen

analyzing the vibration response of the test pipe, and the effectiveness of the nonlinear model is verified. Comparing the calculation results using proposed model and the experimental results, the main frequency and amplitude obtained by the two methods are very similar, which verified the correctness of the nonlinear model of RTS in this paper and lay the foundation for the fatigue reliability analysis of test pipe in Sect. 4.

3 Fatigue life prediction model and S–N curve for test pipe

3.1 Fatigue life prediction model

In this section, the cumulative damage theory (Miner's law) is used to predict the fatigue life of the test pipe [60]. The principle is that when fatigue damage occurs under multi-stage constant amplitude alternating stress, the total damage is the sum of the fatigue damage components under all levels of stress cycles, and the steps of fatigue life analysis are shown as follows.

The stress amplitude of all stress cycles in the service life of the test pipe $(\sigma_1, \sigma_2, \sigma_3 \ldots)$ can be determined by the 3D nonlinear vibration model in Sect. 2, and the corresponding number of cycles $(n_1, n_2, n_3 \ldots)$ can be calculated by the rain flow counting method [61]. The number of cycles of each stress amplitude acting alone $(N_1, N_2, N_3 \ldots)$ can be
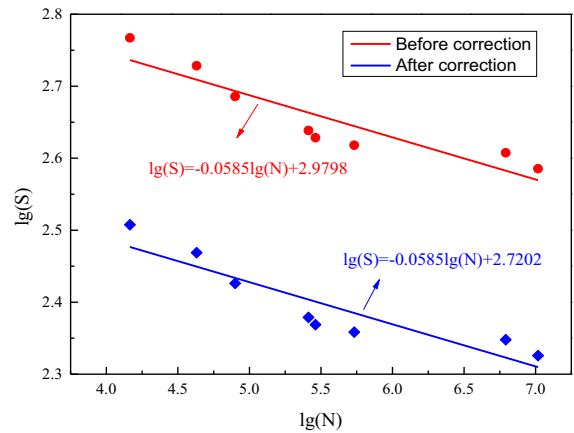

Fig. 17 S–N curve of test pipe material (13Cr-L80)

obtained from the S–N curve of the test pipe. So, the damage degree caused by each stress cycle can be obtained $(^{n_1}/_{N_1}, ^{n_2}/_{N_2}, ^{n_3}/_{N_3} \ldots)$. The total fatigue damage of the test pipe can be obtained by adding all the stress cycle damage, which can be shown as follows:

$$D' = \frac{n_1}{N_1} + \frac{n_2}{N_2} + \frac{n_3}{N_3} + \cdots = \sum_{i=1}^{\infty} \frac{n_i}{N_i} \quad (40)$$

The fatigue life of the test pipe is the reciprocal of the total fatigue damage, which can be shown as follows:

$$T_f = \frac{1}{D'} \quad (41)$$

where T_f is the service life of test pipe and D' is the total fatigue damage.

Finally, the flowchart of fatigue life analysis of test pipe is obtained, as shown in Fig. 13. According to the fatigue life analysis method of test pipe, the S–N curve of pipe material is necessary for the calculation of the fatigue life. Therefore, the next step is to carry out fatigue experiment to determine the S–N curve of the test pipe.

Table 5 Calculation parameters of LS-M well

Parameter	Value	Parameter	Value
Riser and test pipe length (m)	1000	Time step (s)	0.001
Test pipe inner diameter (m)	0.095	Number of division elements	1000
Test pipe outer diameter (m)	0.1143	Friction coefficient	0.243
Riser inner diameter (m)	0.4822	Riser and test pipe density (kg/m^3)	7850
Riser outer diameter (m)	0.533	Seawater density (kg/m^3)	1020
Elastic modulus (GPa)	210	Drilling fluid density (kg/m^3)	1200
Poisson's ratio	0.3	Testing liquid density (kg/m^3)	1120
Random wave height (m)	5–20	Uniform flow velocity (m/s)	0.2–1.1
Random wave period (s)	5	Internal flow velocity (m/s)	5–20
Rotational stiffness of the upper flexible joint (N·m/deg)	8800	Rotational stiffness of the lower flexible joint (N·m/deg)	127,400
Calculation time (s)	50	Top tension coefficient	1.1–1.7
Hard cabin diameter (m)	32.31	Heave plate spacing (m)	23.8
Platform draft (m)	153.924	Total discharge (t)	56,401.45
Depth of platform center (m)	90.39	Number of heave plates	3
Hard cabin length (m)	68.88	Heave linear damping	0.0379
Size of heave plate (m)	32.31 × 32.31	Heave quadratic damping	0.0186

(a) Response of random wave surface **(b)** Wave spectrum **(c)** Heave displacement
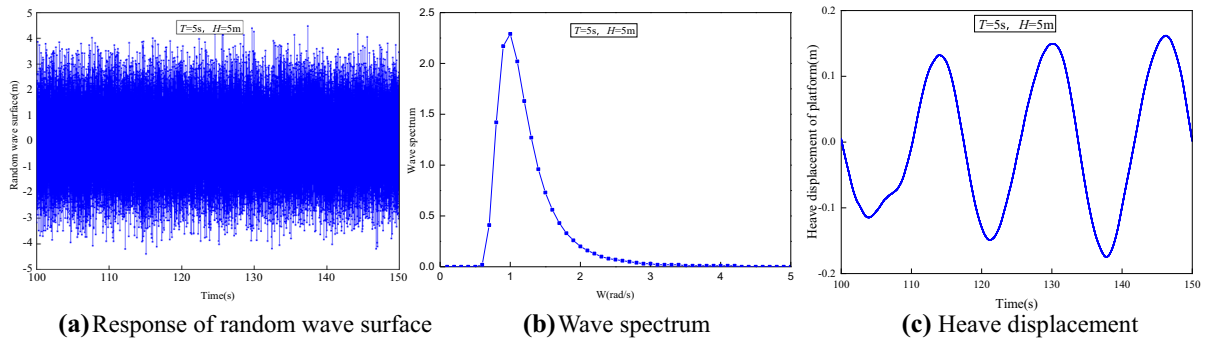
Fig. 18 Time history response of random wave and offshore platform

3.2 Experiment measurement of S–N curve

3.2.1 Equipment of experiment

PQ-6 pure bending fatigue tester is used for this fatigue experiment (Fig. 14), and the working principle of which is that both ends of the test piece are clamped by clamps, and the test load is determined by the weights. So, if the minimum diameter of the specimen is d_{min}, the weight can be calculated by the following formula.

$$F' = \frac{\pi d_{min}^3 \sigma}{16L} - G \tag{42}$$

where F' is weight of loading weight (N); $L = L_1 = L_2$ are arm length (m); σ is stress of test piece (Pa); and G is additional weight including weight plate and force bracket (N).

3.2.2 Experimental procedure

(1) Minimum diameter of test specimen is measuring.

(a) Maximum axial stress   **(b)** Annual fatigue damage rate   **(c)** Fatigue life of test pipe
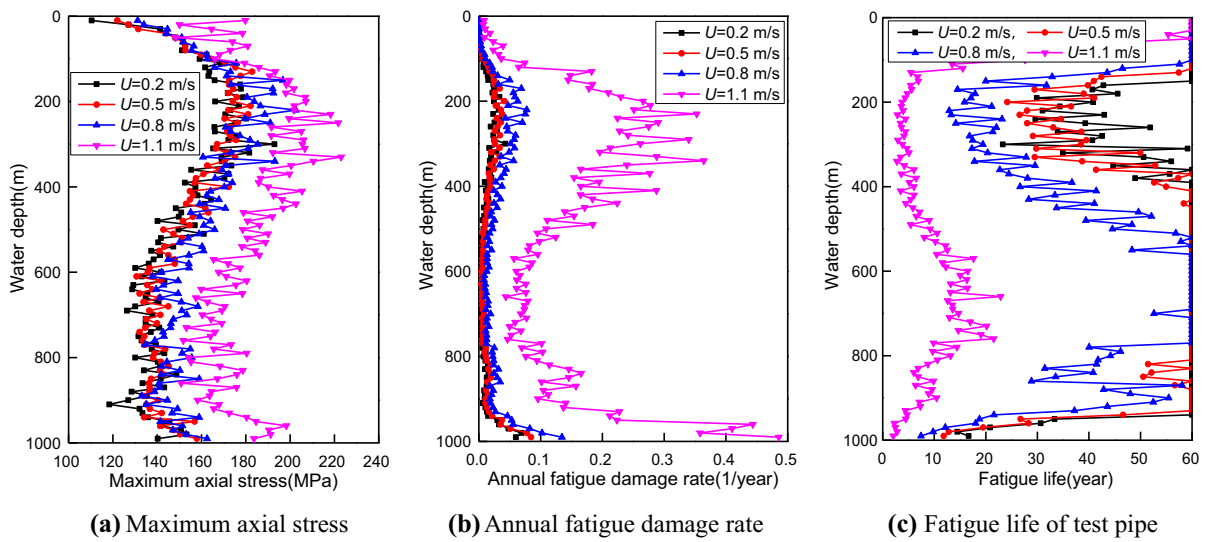
Fig. 19 Fatigue damage analysis data of test pipe under different outflow velocities

(2) According to the determined stress level, calculate the weight of the added weight by Eq. (42), and plus weights.

(3) Lift the weight before starting the machine, add the weight quickly and without impact after the running is stable, and set the counter to zero.

(4) If the sample breaks or the number of tests exceeds 10^7, record the number.

3.2.3 Experimental result

The determination of S–N curve is completed in two parts which are limited fatigue life zone and infinite fatigue life zone, as shown in Fig. 15.

3.2.3.1 Limited fatigue life zone Due to the yield limit of pipe material (13Cr-L80) is 665 MPa, seven stress amplitudes are preliminarily set as 585 MPa, 535 MPa, 485 MPa, 435 MPa, 425 MPa, 415 MPa and 405 MPa. Three test specimens are measured under each stress amplitude, and the number of cycles is recorded when each test specimen is broken. Then, the average number of cycles of three test specimens is taken as the number of cycles corresponding to the stress amplitude, and 21 test specimens are measured in total (Table 2). If the number of cycles of the minimum stress amplitude has not exceeded 10^7, reduce the stress amplitude and continue the test until

the number of cycles is greater than 10^7. Therefore, the S–N curve of finite fatigue life zone can be obtained.

3.2.3.2 Infinite fatigue life zone The initial stress amplitude is determined by the fatigue limit range obtained from the previous test, and the fatigue limit is measured by the lifting method, and the infinite fatigue life zone is obtained by the fatigue limit. According to the judgment of the first sample, if the first sample fails, the stress value will be reduced. Otherwise, it increases (Table 3). The fatigue limit of 13Cr-L80 is calculated from the data of the effective test specimen by Eq. (43), and the S–N curve of the infinite fatigue life zone is obtained.

$$\sigma_{-1} = \frac{1}{9} \times (2 \times 425 + 4 \times 405 + 3 \times 385)$$
$$= 402.78 \, \text{MPa} \tag{43}$$

3.3 S–N curve fitting and correction

After the S–N curve of pipe material is obtained, in order to make the curve more consistent with the actual situation of the field pipe, the S–N curve is corrected from the following four aspects.

3.3.1 Load-type correction factor C_L

In the actual working condition, the test pipe is subject to vertical and horizontal coupling, while the test piece

is subject to pure bending only. Therefore, it is necessary to correct the S–N curve measured in the test, and the correction factor of load type is 0.7 from Table 4.

3.3.2 Test specimen size correction factor C_D

The larger the size of the specimen, the less likely it is to fatigue fracture. The correction factor of test specimen is determined by Eq. (44). In this study, the minimum diameter of the specimen is 6 mm (Fig. 16). Therefore, the size correction factor is 1.0.

$$
\begin{cases}
C_D = 1.0, & d_{\min} < 8 \, \text{mm} \\
C_D = 1.189 \, d - 0.097, & 8 \, \text{mm} < d_{\min} < 250 \, \text{mm}
\end{cases}
\tag{44}
$$

3.3.3 Stress concentration correction factor K_f

Different surface roughness will cause different stress concentration on the surface of the specimen that will affect its fatigue life, and the formula of stress concentration correction factor is put forward by Li [62].

$$
K_f = 1 + \left(1 + 2\sqrt{\lambda_1 R_a / \rho} - 1 \right) q
\tag{45}
$$

where ρ is radius of curvature of the specimen, which is 39 mm (Fig. 16); λ_1 is the ratio of spacing to depth

of micro-cracks, which is 1; q is sensitivity coefficient, which is 0.99; and R_a is the surface roughness of the specimen, which is 6.625 μm measured by a white light interferometer. Therefore, the stress concentration correction factor is 1.0248 by Eq. (45).

3.3.4 Surface quality correction factor C_S

Since the fatigue crack of the test pipe mainly originates on the free surface of the test pipe, the influence of the surface quality of the test specimen on the crack should be considered. According to the test results of surface roughness, it can be seen from the literature [62] that the surface quality correction factor can be 0.82.

After comprehensive consideration of surface roughness, notch effect, loading type, surface quality coefficient and size coefficient, the correction formula is as follows.

$$
S_e = \frac{S_{be} C_L C_S C_D}{K_f} = 0.56 S_{be}
\tag{46}
$$

where S_{be} is standard stress (MPa); S_e is corrected stress (MPa).

Finally, the corrected S–N curve of test pipe material (13Cr-L80) is obtained, as shown in Fig. 17.
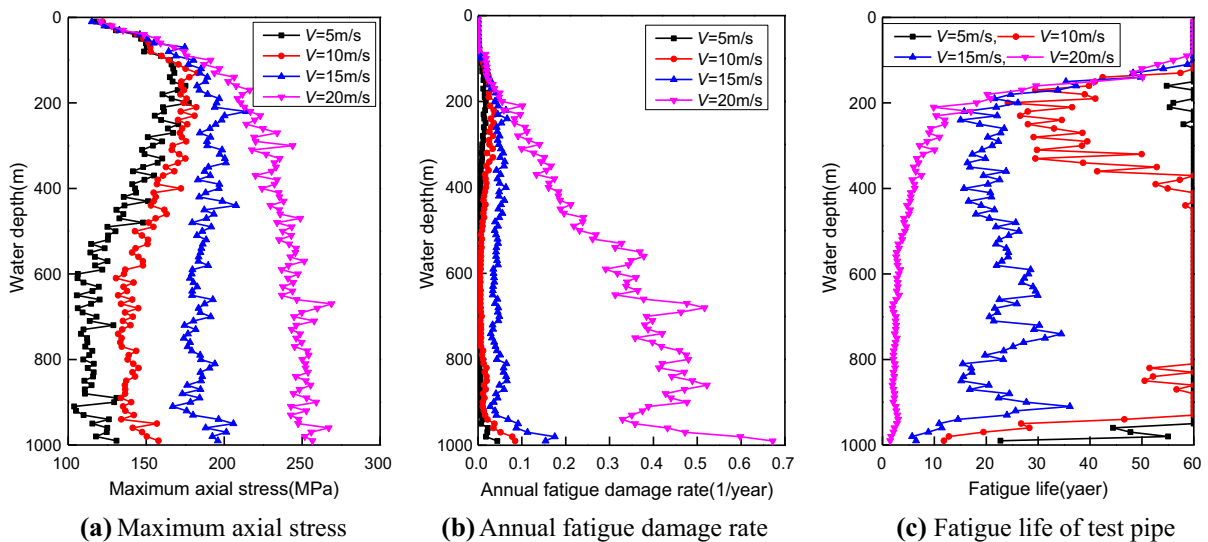

(a) Maximum axial stress   **(b)** Annual fatigue damage rate   **(c)** Fatigue life of test pipe

Fig. 20 Fatigue damage analysis data of test pipe under different internal flow velocities

4 Results and discussion

According to the parameters of LS-M well in the South China Sea (as shown in Table 5) and the proposed nonlinear vibration model in Sect. 2, the influences of external flow velocity, internal flow velocity and top tension coefficient on the stress, fatigue life and fatigue reliability of deepwater test pipe are investigated, and the fatigue failure mechanism of deepwater test pipe is revealed.

According to the established platform heave motion model, the random wave displacement and wave spectrum are calculated. On this basis, the platform heave motion displacement is obtained (as shown in Fig. 18). It can be noted in Fig. 18a, b that random wave presents complex motion state, the amplitude of wave surface motion is less than the wave height of random wave, and the energy of random wave is concentrated between 1 and 1.5 rad/s. It can be observed in Fig. 18c that the heave amplitude of the platform is about 0.15 m. Due to the structure of the platform, it can alleviate the influence of random waves, making its motion relatively slow and regular. The above results lay the foundation of load and displacement boundary for the response analysis of deepwater test pipe.

4.1 Influence of outflow velocity

Under the action of different outflow velocity, the riser presents different vibration states, which affects the vibration characteristics of the test pipe [1, 12, 22]. Therefore, in this study, the outflow velocity is set as 0.2, 0.5, 0.8 and 1.1 m/s, and keeping the internal flow velocity, the top tension coefficient and the significant wave height unchanged, which are, respectively, set as 10 m/s, 1.3 and 5 m. The other calculation parameters are listed in Table 5. The curves of maximum axial stress, annual fatigue damage rate and fatigue life corresponding to different water depths are obtained, as shown in Fig. 19. In order to display the fatigue life of test pipe conveniently, once the fatigue life is more than 60 years, it is considered as 60 years.

It can be seen from Fig. 19a that the maximum alternating stress of the test pipe occurs at the upper "one third" and the bottom positions. The main reason is that the test pipe is affected by the contact/impact force of the outer riser, and its deformation shows the same trend as that of the riser. Meanwhile, the riser is subjected to ocean load, and its maximum stress also appears at the upper "one third" position, which was called "one third effect" by academician Zhou [1]. This is mainly because the ocean load presents a distribution state of large upper end and small lower end, which is similar to the shear distribution. Through the force analysis, its action point is just located at the upper one-third position. At the same time, the
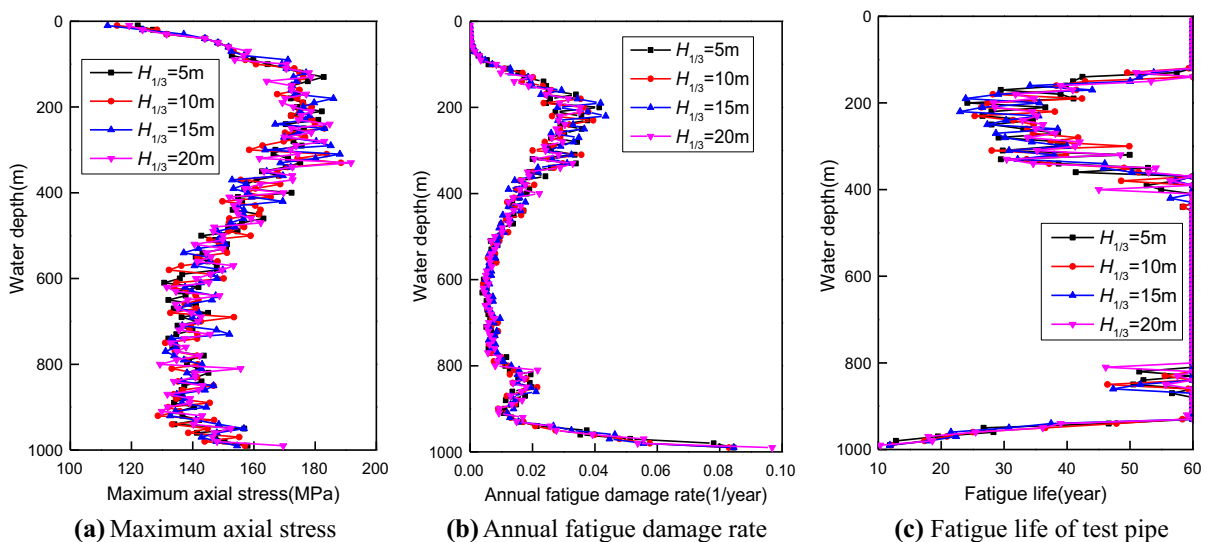

(a) Maximum axial stress   (b) Annual fatigue damage rate   (c) Fatigue life of test pipe

Fig. 21 Fatigue damage analysis data of test pipe under different significant wave heights
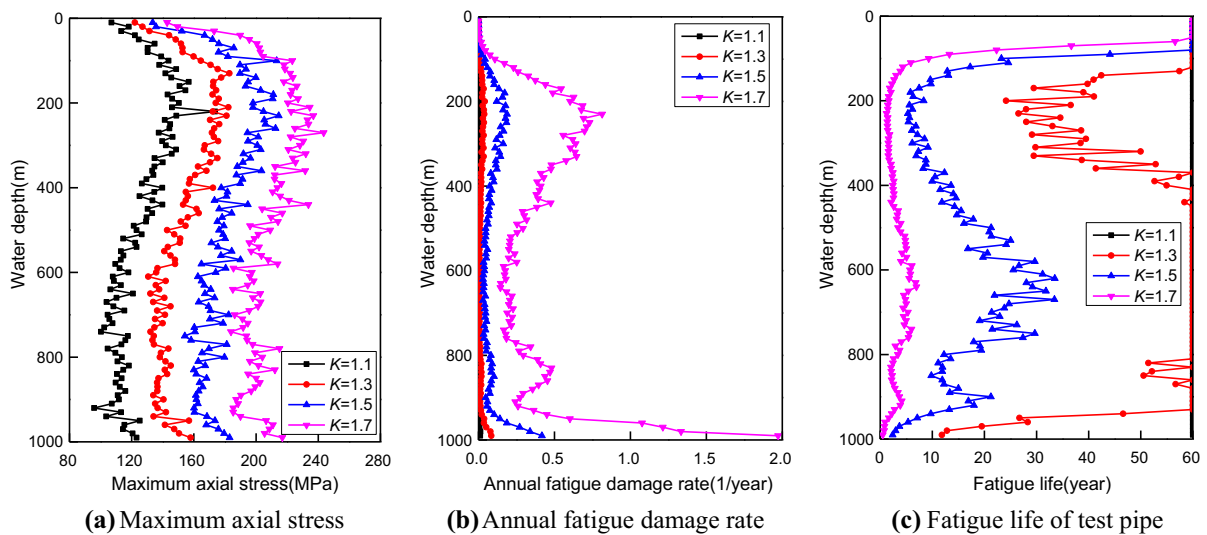
Fig. 22 Fatigue damage analysis data of test pipe under different top tension coefficients

alternating stress at the bottom of the test pipe is also relatively large. The main reason is that during operation, the bottom of test pipe is connected with the lower marine riser packing (LMRP), which limits the axial movement of the test pipe, resulting in concentrated stress at this position. Therefore, the locations where fatigue failure of the test pipe is easy to occur are mainly distributed at the upper "one third" and the bottom of test pipe (as shown in Fig. 19b, c). The service life is about 3 years when outflow velocity is 1.1 m/s, which can meet the requirements of field short-term test (about 2 months). The field designer should pay attention to the fatigue life of the test pipe at this location.

Moreover, it can be observed from Fig. 19 that with the increase in outflow velocity, the maximum alternating stress and annual fatigue damage rate of the test pipe increase. When the flow velocity is small (lower than 0.8 m/s), the increasing trend is not obvious, but when the flow velocity is large (higher than 0.8 m/s), the alternating stress of the test pipe varies significantly. As a result, the annual fatigue damage rate also increased significantly and the service life decreased significantly (from 8 to 3 years). The main reason is that the increase in the outflow velocity leads to the increase in the marine load and the increase in the vibration of the riser. The alternating stress of the internal test pipe also increases through the contact/collision transmission effect. When the velocity continues to increase, the dominant frequency of the

external excitation is close to that of the riser, and the riser has a resonance effect, resulting in a significant increase in the alternating stress. Finally, the alternating stress of the internal test pipe also increases significantly. Therefore, in the process of field operation, in case of severe offshore conditions (with large outflow velocity), other measures need to be taken to reduce the vibration of the test pipe (such as changing the flow velocity and top tension coefficient) to improve its fatigue life.

4.2 Influence of internal flow velocity

Deepwater testing process is an important process to detect the safety of oil and gas production in the later stage. Testing the safety of the whole oil and gas production system at different flow velocity in the test pipe can lay a foundation for the allocation of oil and gas well production in the later stage. Therefore, the internal flow velocity is an important index in the testing process. In this study, the internal velocity is set as 5, 10, 15 and 20 m/s, and keeping the outflow velocity, the top tension coefficient and the significant wave height unchanged, which are, respectively, set as 0.5 m/s, 1.3 and 5 m. The other calculation parameters are listed in Table 5. The curves of maximum axial stress, annual fatigue damage rate and fatigue life corresponding to different water depths are obtained, as shown in Fig. 20.

It can be noted in Fig. 20a that, with the increase in flow velocity in the test pipe, the alternating stress at the lower part of the test pipe increases significantly, and this increasing trend decreases in turn with the seabed to the wellhead. The main reason is that the action load of internal fluid on the test pipe mainly occurs at the position with large transverse deformation. Under the action of the test pipe self-gravity, the lower pipe string is subjected to axial compression load, which presents a certain bending state. That results in a large flow force when the fluid in the pipe flows through these positions. Meanwhile, the upper test pipe is tensioned under its self-gravity action, and the fluid excitation is very small. Therefore, with the increase in flow velocity, the change trend of alternating stress of the test pipe at the upper is very small. Finally, it can be seen that with the increase in internal flow velocity, the "one third effect" of the test pipe will decrease, and it shows "the bottom damage effect", which needs the attention of field operators.

It can be stated from Fig. 20b, c that when the internal flow velocity is 5 m/s and 10 m/s, the maximum annual fatigue damage rate of the test pipe occurs at the upper "one third" and the bottom position, where the fatigue life is small, about 22 years and 12 years, respectively. With the increase in the internal flow velocity to 15 m/s and 20 m/s, the annual fatigue damage rate of the test pipe at the bottom position is significantly greater than that at the middle and upper position, and the life decreases significantly, about 5 years and 1.5 years, respectively. Therefore, during field operation, when low flow velocity is configured in the test pipe, it is necessary to focus on the fatigue damage at the upper "one third" and bottom position of the test pipe. When high flow velocity is configured in the test pipe, it is necessary to focus on the fatigue damage at the bottom position of the test pipe. The research results of this study provide a theoretical basis for field operation and parameter design.

4.3 Influence of significant wave height

The marine random wave mainly affects the heave motion of the platform and then affects the vibration characteristics of the test pipe. By exploring the influence rules of the different significant wave height of marine random wave on the fatigue damage of deepwater test pipe, it can effectively guide the specific operations to be carried out on site under different sea conditions. Therefore, in this study, the significant wave height is set as 5, 10, 15 and 20 m, and keeping the outflow velocity, the top tension coefficient and the internal velocity unchanged, which are respectively set as 0.5 m/s, 1.3 and 10 m. The other calculation parameters are listed in Table 5. The curves of maximum axial stress, annual fatigue damage rate and fatigue life corresponding to different water depths are obtained, as shown in Fig. 21.

It can be seen from Fig. 21a, b, c that, with the increase in ocean random wave height, the alternating stress of the test pipe decreases first and then increases, but the variation amplitude is not very obvious. The main reason is that with the increase in random wave height, the heave amplitude of the platform increases, which increases the displacement of the upper end of the test pipe. On the one hand, it can effectively reduce the transverse vibration of the test pipe. On the other hand, it increases the axial stress of the test pipe. When the random wave height increases slightly, the decrease trend of transverse vibration is greater than the increase trend of axial stress. The axial alternating stress of the test pipe is effectively reduced. However, when the random wave height increases again, the decreasing trend of transverse vibration is less than the increasing trend of axial stress, resulting in the increase in axial alternating stress of the test pipe. Moreover, with the increase in ocean random wave height, the annual fatigue damage rate of the test pipe first decreases and then increases, while its fatigue life first increases and then decreases. Their variation amplitude trend is similar to that of the alternating stress of the test pipe, which indicated that the increase in ocean random wave height does not affect the vibration frequency of the deepwater test pipe. The change of fatigue damage of test pipe is mainly caused by the variation of alternating stress. Therefore, during field operation, when the sea random wave height is large, it is necessary to set other parameters (such as reducing the internal flow velocity and configuring appropriate top tension coefficient) to improve the fatigue life of the test pipe.

4.4 Influence of top tension coefficient

Tensioner is an important component of deepwater RTS and the only connecting component between drilling platform and submarine system. Top tension

coefficient is an important mechanical parameter of tensioner, and its value determines the top tension. Different top tension will affect the vibration characteristics of deepwater test pipe, resulting in the change of its fatigue characteristics. Therefore, the influence of different top tension coefficients on fatigue damage of deepwater test pipe is explored to guide the configuration of top tension coefficient on site. In this study, the top tension coefficient is set as 1.1, 1.3, 1.5 and 1.7, and keeping the outflow velocity, the internal velocity and the significant wave height unchanged, which are, respectively, set as 0.5 m/s, 10 m/s and 5 m. The other calculation parameters are listed in Table 5. The curves of maximum axial stress, annual fatigue damage rate and fatigue life corresponding to different water depths are obtained, as shown in Fig. 22.

It can be observed from Fig. 22a that, with the increase in the top tension coefficient, the alternating stress of the test pipe increases, and the increasing range of the alternating stress of the test pipe along the water depth direction is similar. The main reason is that with the increase in the top tension coefficient, the top tension applied by the tensioner increases, resulting in the riser being pulled tighter. Under the action of transverse ocean load, the contact and collision effect between the riser and the test pipe is more obvious, and finally, the axial alternating stress of the riser increases. Moreover, it can be observed from Fig. 22b that, with the increase in the top tension coefficient, the annual fatigue damage rate of the test pipe shows an increasing trend, but which increases more and more obviously, showing an uneven increasing trend. The increasing trend of annual fatigue damage rate is different from that of alternating stress of test pipe. The main reason is that with the increase in the top tension coefficient, on the one hand, the alternating stress of the test pipe is increased. On the other hand, when the test pipe is pulled tighter, its vibration frequency will also increase under the same external force, and this increasing trend becomes more obvious with the increase in the top tension coefficient. It can be stated from Fig. 22c that when the top tension coefficient changes from 1.3 to 1.5, the fatigue life of the test pipe decreases significantly, and the minimum fatigue life is about 2.5 years. When the top tension coefficient is 1.7, the fatigue life of the test pipe is about 0.6 years, and the test pipe is in a serious dangerous state. Therefore, during field operation, it is

necessary to properly configure the top tension coefficient so that there can be a certain relaxation between the riser and the test pipe, so as to cause transverse vibration and consume some axial energy and load.

5 Conclusions

(1) The three-dimensional (3D) nonlinear vibration model of deepwater RTS is established using the micro-finite method, energy method and Hamilton variational principle. In the model, the vortex-induced effect on riser, flow-induced effect on test pipe and longitudinal/transverse coupling effect are taken into account. Based on the elastic–plastic contact collision theory, the nonlinear contact load calculation method between riser and test pipe is proposed. Due to too many nonlinear factors considered in the 3D nonlinear vibration model, the incremental Newmark-β method and Newton–Raphson method are used to solve the model simultaneously.

(2) Based on field parameters of BY-M gas well in deepwater block of South China Sea and simulation experiment area conditions, the vibration simulation test bench of the RTS is designed using geometric similarity, motion similarity and dynamic similarity. The vibration simulation experiment of the RTS is carried out, and the vibration response data of RTS are measured. Compared with experimental measurement results, calculation results of the proposed vibration model in this study and the single tubing vibration model in our recent work, the results demonstrate that the calculated results using the proposed model are basically consistent with the experimental data in amplitude and frequency, while the calculated results using the single-tube model are quite different from the experimental data, which verifies the correctness and effectiveness of the nonlinear vibration model of the RTS.

(3) The cumulative damage theory (Miner's law) is used to establish the fatigue life prediction method of test pipe combined with the stress response which was determined by the proposed

3D nonlinear model and the S–N curve of the tubing material (13Cr-L80) which was measured by fatigue test. Based on that, according to the parameters of LS-M well in the South China Sea, the influences of external flow velocity, internal flow velocity and top tension coefficient on the stress, fatigue life and fatigue reliability of deepwater test pipe are investigated.

(4) The results obtained demonstrate that, first, with the increase in outflow velocity, the maximum alternating stress, the annual fatigue damage rate increased and the service life decreased significantly. The locations where fatigue failure of the test pipe is easy to occur are mainly distributed at the upper "one third" and the bottom of test pipe. Second, with the increase in internal flow velocity, the "one third effect" of the test pipe will decrease, and it shows "the bottom damage effect", which needs the attention of field operators. Third, during field operation, it is necessary to properly configure the top tension coefficient so that there can be a certain relaxation between the riser and the test pipe, so as to cause transverse vibration and consume some axial energy and load.

Data availability The authors declare that the data supporting the findings of this study are available within the article.

Declarations

Conflict of interest The authors declare that there are no conflicts of interest regarding the publication of this paper.

References

1. Zhou, S., Liu, Q., Jiang, W., Mao, L., Yang, X., Liu, Z., Wang, G., Huang, X., Shi, X.: The discovery of "one third effect" for deep water drilling riser: based on the theoretical and experimental study of the deformation characteristics of deep water drilling riser by ocean currents. China Offshore Oil Gas **25**(6), 1–7 (2013)
2. Sarpkaya, T.: Vortex-induced oscillations-a selective review. J. Appl. Mech. **46**(2), 241–258 (1979)
3. Bearman, P.W.: Vortex shedding from oscillating bluff bodies. Annu. Rev. Fluid Mech. **16**(1), 195–222 (2003)
4. Dahl, J.M., Hover, F.S., Triantafyllou, M.S., Oakley, O.H.: Dual resonance in vortex-induced vibrations at subcritical and supercritical reynolds numbers. J. Fluid Mech. **643**(3), 395–424 (2010)
5. Facchinetti, M.L., Langre, E.D., Biolley, F.: Coupling of structure and wake oscillators in vortex-induced vibrations. J. Fluids Struct. **19**(2), 123–140 (2004)
6. Vandiver, J.K., Jaiswal, V., Jhingran, V.: Insights on vortex-induced, traveling waves on long risers. J. Fluids Struct. **25**(4), 641–653 (2009)
7. Huera-Huarte, F.J., Bangash, Z.A., González, L.M.: Towing tank experiments on the vortex-induced vibrations of low mass ratio long flexible cylinders. J. Fluids Struct. **48**, 81–92 (2014)
8. Gao, Y., Fu, S., Wang, J., Song, L., Chen, Y.: Experimental study of the effects of surface roughness on the vortex-induced vibration response of a flexible cylinder. Ocean Eng. **103**(1), 40–54 (2015)
9. Bourguet, R., Karniadakis, G.E., Triantafyllou, M.S.: Vortex-induced vibrations of a long flexible cylinder in shear flow. J. Fluid Mech. **677**(677), 342–382 (2011)
10. Bourguet, R., Karniadakis, G.E., Triantafyllou, M.S.: Distributed lock-in drives broadband vortex-induced vibrations of a long flexible cylinder in shear flow. J. Fluid Mech. **717**(1), 361–375 (2013)
11. Mao, L., Zeng, S., Liu, Q.: Dynamic mechanical behavior analysis of deep water drilling riser under hard hang-off evacuation conditions. Ocean Eng. **183**, 318–331 (2019)
12. Mao, L., Zeng, S., Liu, Q., Wang, G., He, Y.: Dynamical mechanics behavior and safety analysis of deep water riser considering the normal drilling condition and hang-off condition. Ocean Eng. **199**, 106996 (2020)
13. Mathelin, L., Langre, E.: Vortex-induced vibrations and waves under shear flow with a wake oscillator model. Eur. J. Mech. B. Fluids **24**(4), 478–490 (2005)
14. Khalak, A., Williamson, C.H.K.: Motions, forces and mode transitions in vortex-induced vibrations at low mass-damping. J. Fluids Struct. **13**(7–8), 813–851 (1999)
15. Xu, J., Wang, D., Huang, H., Duan, M., Gu, J., An, C.: A vortex-induced vibration model for the fatigue analysis of a marine drilling riser. Ships Offshore Struct. **12**(sup1), S280–S287 (2017)
16. He, F., Dai, H., Huang, Z., Wang, L.: Nonlinear dynamics of a fluid-conveying pipe under the combined action of cross-flow and top-end excitations. Appl. Ocean Res. **62**, 199–209 (2017)
17. Jauvtis, N., Williamson, C.H.K.: Vortex-induced vibration of a cylinder with two degrees of freedom. J. Fluids Struct. **17**(7), 1035–1042 (2003)
18. Gu, J., Yang, C., Zhu, X.Y., Wu, J.: Influences of mass ratio on vortex induced vibration characteristics of a circular cylinder. J. Vib. Shock **35**(4), 134–140 (2016)

19. Martins, F.A.C., Avila, J.P.J.: Effects of the Reynolds number and structural damping on vortex-induced vibrations of elastically-mounted rigid cylinder. Int. J. Mech. Sci. **156**, 235–249 (2019)

20. Gao, G., Cui, Y., Qiu, X., Shu, Q.: Parameter influencing analysis of vortex-induced vibration response of deep sea top tensioned riser. Shipbuild. Eng. **41**(2), 101–107 (2019)

21. Liu, J., Zhao, H., Liu, Q., He, Y., Wang, G., Wang, C.: Dynamic behavior of a deepwater hard suspension riser under emergency evacuation conditions. Ocean Eng. **150**, 138–151 (2018)

22. Liu, J., Guo, X., Liu, Q., Wang, G., He, Y., Li, J.: Vortex induced vibration response characteristics of marine riser considering the in-line and cross-flow coupling effect. Acta Pet. Sin. **40**(10), 1270–1280 (2019)

23. Aitken, J.: An account of some experiments on rigidity produced by centrifugal force. Phil. Mag. **5**, 81–105 (1878)

24. Shilling, R., Lou, Y.K.: An experimental study on the dynamic response of a vertical cantilever pipe on the dynamic response of a vertical cantilever pipe conveying fluid. J. Energy Res. Technol. **102**, 129–135 (1980)

25. Deng, Y.Z.: Vibration mechanism analysis and fatigue life prediction of tubing string in high yield gas well. Southwest Petroleum University (2006)

26. Paidoussis, M.P., Luu, T.P., Prabhakar, S.: Dynamics of a long tubular cantilever conveying fluid downwards, which then flows upwards around the cantilever as a confined annular flow. J. Fluids Struct. **24**(1), 111–128 (2008)

27. Ju, Q.L., Tong, S.K.: Analysis of vertical vibration characteristics of completion string of high yield gas well. Drill. Prod. Technol. **37**(02), 79–82+119–120 (2014)

28. Zhang, Q., Miska, S.: Lateral vibration of nonrotating drill pipe conveying fluid in vertical holes. In: Asme/jsme joint fluids summer engineering conference, pp. 109–120 (2003)

29. Bagdatli, S.: Non-linear transverse vibrations of tensioned nanobeams using nonlocal beam theory. Struct. Eng. Mech. **55**(2), 281–298 (2015)

30. Dai, H.L., Abdelkefi, A., Wang, L.: Modeling and nonlinear dynamics of fluid-conveying risers under hybrid excitations. Int. J. Eng. Sci. **81**, 1–14 (2014)

31. Yu, K.Q.: Fluid solid coupling vibration analysis and safety evaluation of completion string of high production gas well. Xi'an University of petroleum (2017)

32. Xing, Y.F., Liang, K.: Nonlinear vibration analysis of longitudinal-transverse coupled beam. J. Beijing Univ. Aeronaut. Astronaut. **41**(08), 1359–1366 (2015)

33. Li, Z.F.: Research advances and debates on tubular mechanics in oil and gas well. Acta Pet. Sin. **37**(4), 531–556 (2016)

34. Liu, J., Zhao, H., Yang, S., Liu, Q., Wang, G.: Nonlinear dynamic characteristic analysis of a landing string in deepwater riserless drilling. Shock Vib. (2018). https://doi.org/10.1155/2018/8191526

35. Wang, W.M., Xiong, M.H., Chen, Q.R., Chen, Y.C., Zhang, S.M., Yang, D.F.: Simulation analysis of load transfer in deep sea pipe-in-pipe vertical system. Oil Field Equip. **3**, 1–5 (2015)

36. Li, C.N.: Buckling of concentric string pipe-in-pipe. SPE-187445-MS (2017)

37. Liu, K., Chen, G.M., Chang, Y.J., Zhu, B.R., Liu, X.Q.: Nonlinear dynamic analysis and fatigue damage assessment for a deepwater test string subjected to random loads. Pet. Sci. **13**(1), 126–134 (2016)

38. Yang, M.J., Li, H.T., Jiang, R., Xiao, K.W., Xie, J.: Research on vibration damage of completion string in Yolotan high-yield gas well. J. Southwest Pet. Univ. (Sci. Technol. Ed.) **38**(01), 158–163 (2016)

39. Liu, J., Guo, X., Wang, G., Liu, Q., Fang, D., Huang, L., Mao, J.: Bi-nonlinear vibration model of tubing string in oil&gas well and its experimental verification. Appl. Math. Model. **81**, 50–69 (2020)

40. Guo, X., Liu, J., Wang, G., Dai, L., Fang, D., Huang, L.: Nonlinear flow-induced vibration response characteristics of a tubing string in HPHT oil&gas well. Appl. Ocean Res. **106**, 102468 (2021)

41. Drumond, G.P., Pasqualino, I.P., Pinheiro, B.C., Estefen, S.F.: Pipelines, risers and umbilicals failures: a literature review. Ocean Eng. **148**, 412–425 (2018)

42. Lekkala, M.R., Mohamed, L., Hafiz, M.F.U., Kim, D.K.: A practical technique for hydrodynamic coefficients modification in SHEAR7 for fatigue assessment of riser buoyancy modules under vortex-induced vibration. Ocean Eng. **217**, 107760 (2020)

43. Chen, S.S., Wang, H.X., Liu, Y.X., Lan, W.J., Lv, X.X., Sun, B.Y.: Root cause analysis of tubing and casing failures in low-temperature carbon dioxide injection well. Eng. Fail. Anal. **104**, 873–886 (2019)

44. Hejazi, R., Grime, A., Randolph, M., Efthymiou, M.: A Bayesian machine learning approach to rapidly quantifying the fatigue probability of failure for steel catenary risers. Ocean Eng. **235**, 109353 (2021)

45. Chen, R.F., Low, Y.M.: Efficient long-term fatigue analysis of deepwater risers in the time domain including wave directionality. Mar. Struct. **78**, 103002 (2021)

46. Zhao, H.L.: Study on the Mechanism of Vortex -Induced Vibration of Marine Riser Under the Influence of Nonlinear Factors. Southwest Petroleum University, Chengdu (2019)

47. Xu, B.Y.: Elastoplastic Mechanics and its Application. China Machine Press, Beijing (1984)

48. Violette, R., Langre-e, D.E., Szydlowski, J.: Computation of vortex-induced vibrations of long structures using a wake oscillator model: comparison with DNS and experiments. Comput Struct. **85**(11–14), 1134–1141 (2007)

49. Wen, S.T., Huang, P., Tian, Y., Ma, L.R.: Principles of Tribology, 5th edn. Tsinghua University Press, Beijing (2018)

50. Guo, X., Liu, J., Dai, L., Liu, Q., Fang, D., Wei, A., Wang, J.: Friction-wear failure mechanism of tubing strings used in high-pressure, high-temperature and high-yield gas wells. Wear Mar. **468–469**, 203576 (2021)

51. Luo, T.: Fluid Mechanics. Machinery Industry Press, Beijing (2017)

52. Liu, Q.Y., He, Y.F.: Mechanical Behavior of Injection String in Deep Well and its Application. Science Press, Beijing (2013)

53. Mao, L., Liu, Q., Zhou, S., Wang, G., Fu, Q.: Deep water drilling riser mechanical behavior analysis considering actual riser string configuration. J. Nat. Gas Sci. Eng. **33**, 240–254 (2016)

54. Shen, W.J.: Study on the Nonlinear Stochastic Dynamic Response Characteristics of a Truss Spar. Tianjin University, Tianjin (2012)

55. Longuet-Higgins, M.S.: The effect of non-linearities on statistical distributions in the theory of sea waves. J. Fluid Mech. **17**(03), 459–480 (1963)

56. Guo, X.Q., Li, X., Liu, J., Dai, L.M., Huang, L., Wei, A.C., Zhang, X.H.: Fatigue failure mechanism of 3D tubing strings used in high-pressure, high-temperature and high-yield curved gas wells. Eng. Fail. Anal. **128**, 105536 (2021)

57. Tang, Y.G., Pan, Y.R., Zhang, J., Wang, B.: Experiment on vortex induced vibration of deep sea risers considering parametric excitations. J. Tianjin Univ. **49**(1), 58–64 (2016)

58. Li, Z.F., Wang, C.J., Tian, W.C., Xie, J.: Three principles of drill string mechanics and qualitative simulation experiments. Acta Pet. Sin. **38**(2), 227 (2017)

59. Cardarelli, F.: Materials Handbook. A Concise Desktop Reference, 3rd edn. Springer, Cham (2018)

60. Zhang, T.: Review on research and development of fatigue life analysis methods. Agric. Equip. Veh. Eng. **56**(11), 91–93 (2018)

61. Li, B.: Application of rain flow counting method in structural fatigue damage calculation. Sci. Technol. Horiz. **16**, 190–244 (2015)

62. Li, Y.L.: Theory and Practice of Fatigue Test Analysis. Trans. Zhang Ranzhi. Beijing, National Defense Industry Press, pp. 102–110 (2011)